THESIS

Study of pendulum thermal noise in gravitational wave detectors

重力波検出器における振り子の熱雑音の研究

Kazuhiro Agatsuma

我妻 一博

Department of Physics, Faculty of Science,
University of Tokyo,
東京大学大学院　理学系研究科　物理学専攻

December 2009

Abstract

We have studied the pendulum thermal fluctuation caused by induced currents, which are a type of the viscous damping, in the CLIO (Cryogenic Laser Interferometer Observatory) gravitational wave detector . This thesis focuses on conductors around magnets glued onto a mirror as the thermal noise sources. There are two conductive parts near each mirror in a gravitational wave detector: the coil circuits and coil holder. The coil circuit is a part of a coil-magnet actuator used in the operation of the interferometer. That coils are supported by the coil holder. The sensitivity of the CLIO interferometer was improved, by replacing a conductive coil holder with an electrically isolated one. I confirmed that the noise spectrum of the CLIO sensitivity almost agreed with the theoretical estimate using the fluctuation-dissipation theorem (FDT). Moreover, we directly measured the pendulum thermal fluctuation due to the coil circuit in an off-resonant and wide-frequency region. The shift of the noise floor was observed as the dissipation was changed by using three patterns of coil-circuit resistances. These measurements well agreed with the theoretical prediction, which was derived by the FDT. In other words, this is the first time that the FDT for the mechanical systems has been validated experimentally above the resonance frequency. Owing to this study, it was found that the coil circuits in the old setup also caused the thermal noise that was comparable with the design sensitivity in CLIO. The thermal noise from the coil circuits were reduced by decreasing the actuator response and increasing the output impedance of the coil driver.

Contents

Chapter 1

Introduction

Gravitational waves (GWs) were predicted by A. Einstein from the general theory of relativity in 1916 [1]. GWs are ripples of space-time with the velocity of light, which are emitted by the accelerative motion of mass, analogous to the emission of electromagnetic waves due to the accelerative motion of charged particles. Because the interaction between matter and GWs is extremely weak, it is thought that observable GWs are only caused by astronomical events.

R. A. Hulse and J. H. Taylor [2] observed that the orbital period of a binary pulsar (PSR 1913+16) decreased over time. The change in the orbital period agreed well with that calculated from relativity, in which it is assumed that energy is emitted by GWs. This result indirectly proved the existence of GWs, and Hulse and Taylor received the Nobel Prize in Physics in 1993.

However, nobody has ever observed GWs "directly". The direct observation of GWs would not only experimental check of Einstein's prediction, but also allow the use of new techniques in astronomy using GWs. Sources of GWs are thought to include the coalescence of binary pulsars, a supernovas, black holes, and the inflation of the universe. There are some phenomena that can not be observed by electromagnetic waves and neutrinos, but only GWs. The direct observation of GWs would contribute to progress in both astronomy and cosmology.

Studies on the direct observation of GWs have been carried out. The sensitivity and observable frequency range of GW detectors have improved over time. In the United States of America, there are GW detectors of LIGO (Laser Interferometer Gravitational Wave Observatory) [3] project, which are composed of two laser interferometers with 4 km arms and one with 2 km arms. In Italy, there is a GW detector of VIRGO (named after the Virgo cluster) [4] project that has a 3-km-long interferometer. In Germany, the GW detector GEO600 [5] has a 600-m-baseline interferometer. In Australia, the AIGO (Australian International Gravitational Observatory) [6] project is currently being discussed as a future project.

In Japan, there are two GW detectors [7]. One is TAMA300 [8, 9], which is located in the National Astronomical Observatory of Japan in Mitaka, near Tokyo. The other is CLIO (Cryogenic Laser Interferometer Observatory) [10, 11, 12, 13], which is placed in the Kamioka Observatory in Gifu prefecture. CLIO is a prototype interferometer for the next Japanese GW telescope project LCGT (Large-scale Cryogenic Gravitational-wave Telescope) [14]. The main goal of CLIO is to demonstrate an improved sensitivity through the reduction of thermal noise by cooling the mirrors. GW detectors must have ultraprecise sensitivity. Therefore, despite its small quantity, even the thermal fluctuation in GW detectors is a matter of concern. GW detectors consist of mirrors suspended by pendulums to bring them close to a state of free mass. Thermally excited mechanical vibrations of the mirrors themselves and their suspensions may determine the fundamental limits of GW detectors.

Direct observations of the thermal fluctuation of the mirror have been performed by Numata et al. [15] and Black et al. [16]. They identified the thermal fluctuation using the fluctuation-dissipation theorem (FDT) [17, 18], which was used to evaluate the fluctuation from the dissipation in thermal equilibrium. In these experiments, the thermal fluctuation of the pendulum could not be observed, because the seismic noise and mirror thermal fluctuation had large amplitudes. The level of seismic noise was higher than that

of pendulum thermal fluctuation below the frequency of 100 Hz. The mirror thermal fluctuation was also larger than the pendulum thermal fluctuation above 10 Hz, because a small spot size (radii of 49 μm and 85 μm in Numata et al. [15] and 160 μm in Black et al. [16]) was used on the mirror surface to increase the mirror thermal fluctuation.

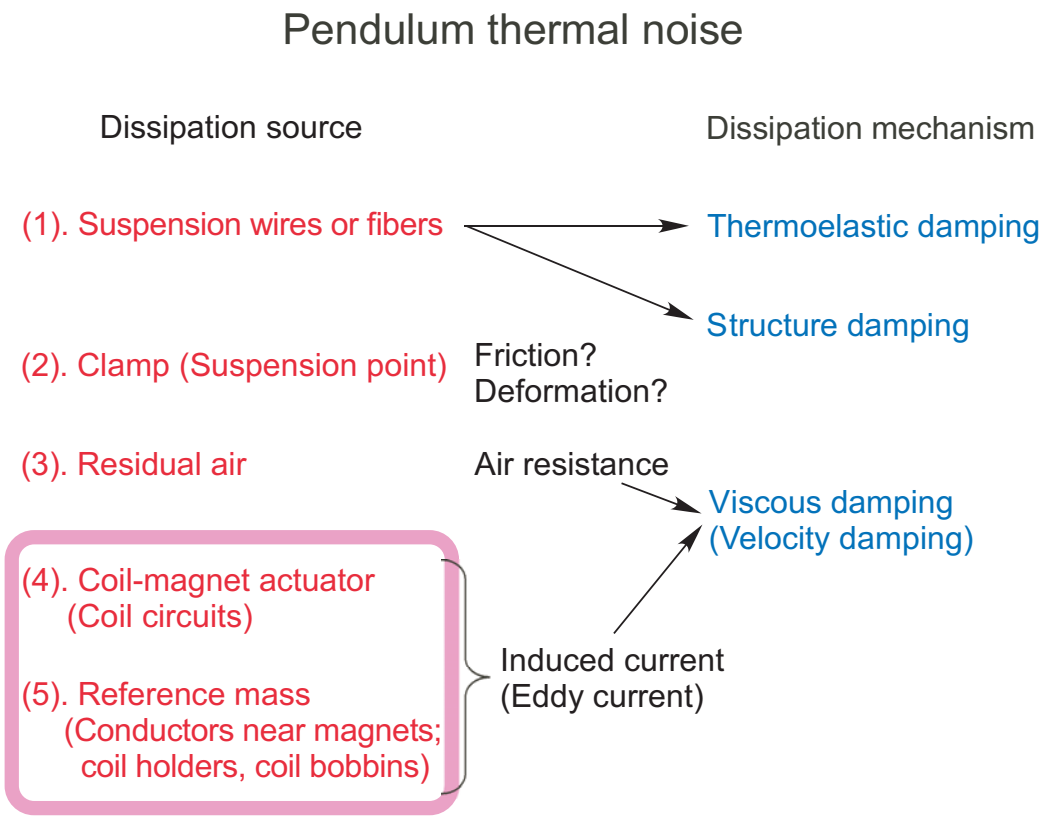

Figure 1.1: Categories of pendulum thermal noise. Sources (4) and (5) are focused on in this thesis.

Pendulum thermal fluctuation is caused by several sources of dissipation that couple with the whole pendulum. Studies heve been performed on the following sources of dissipation: internal loss in materials used as suspension wires [19, 20], clamps of wires [21], residual air [19, 22, 23], coil-magnet actuators [24], and a reference mass with coils [25, 26]. Figure 1.1 shows the different categories of pendulum thermal noise. In the past, thermal

noise due to eddy currents ((4) and (5) in Fig. 1.1) was sufficiently large to compromise the design sensitivity of CLIO in the low-frequency region.

Through noise hunting, the sensitivity of CLIO was drastically improved. One of the most important improvement was to get rid of pendulum thermal noise by the coil holder ((5) in Fig. 1.1). We have verified the pendulum thermal noise both theoretically and an experimentally. This result led to a direct verification of the noise spectra estimated by Cagnoli et al. [25] and Frasca et al. [26].

Furthermore, we performed a quantitative experiment to identify the pendulum thermal noise due to induced currents. Identification of the pendulum (mechanical harmonic oscillator) thermal noise has so far been limited to a region with a width of only several times the resonance frequency [20, 22, 27]. In our experiment we measured the pendulum thermal fluctuation in an off-resonant region and also in a wideband region of over one decade, which is close to the most likely band in which GWs are expected to be detected (around 100 Hz). This was the first successful identification of thermal fluctuation above the resonance frequency in a wide frequency region. The observed fluctuations were extremely small value of about $2 \times 10^{-18}\,\mathrm{m}/\sqrt{\mathrm{Hz}}$ at 100 Hz. The seismic noise was reduced by the quiet environment; CLIO is located 1000 m underground. The mirror thermal noise was also reduced owing to the large spot size (radii of 4.9 mm and 8.5 mm, at which the electric field decreased by a factor of 1/e) of the laser on the mirror surface. The quality factors of our pendulums using 1.8 kg mirrors were on the order of 10^5, and were not smaller than those of the current km-scale interferometer pendulums [3, 4]. To identify the thermal fluctuation of the pendulum, we made use of coil-magnet actuators, which had a number of merits: One was that the dissipation that occurred in the coil circuits was easy to control and analyze. Another was that all of the parameters were measurable. Moreover, the coil-magnet actuators did not cause any modification of the interferometer components with changes in the dissipation in the coil circuits. These merits allowed us to perform a highly reliable experiment.

The contents of this thesis are as follows. In Chapter 2, the methods used to detect GWs and various GW detectors currently in use are introduced briefly. In Chapter 3, the theoretical calculation of pendulum thermal noise is reviewed as the background to the main theme in this thesis. In Chapter 4, the GW detector CLIO is described. The main experiment was performed at CLIO, which was used as a displacement sensor to detect pendulum thermal fluctuation. In Chapter 5, the experiment on the main theme in this thesis, the identification of pendulum thermal noise, is described. Two results related to sources (4) and (5) in Fig. 1.1 are given. The conclusion of this thesis is given in Chapter 6.

Chapter 2

Detection of gravitational waves

2.1 Gravitational waves

According to the theory of general relativity, the distance between a space-time point, x^μ, and a different point separated by an infinitesimal distance, dx, is defined as

$$ds^2 = g_{\mu\nu} dx^\mu dx^\nu. \tag{2.1}$$

Here, μ and ν are numbers from 0 to 3, so that $x^\mu = (x^0, x^1, x^2, x^3) = (-ct, x, y, z)$. $g_{\mu\nu}$ is a metric tensor of space-time. The metric tensor, which expresses the curvature of space-time, can be obtained from the solution of the Einstein equation

$$R_{\mu\nu} - \frac{1}{2} g_{\mu\nu} R = \frac{8\pi G}{c^4} T_{\mu\nu}. \tag{2.2}$$

Here, G is the gravitational constant, c is the light velocity, $R_{\mu\nu}$ is the Ricci tensor, R is the Ricci scalar, and $T_{\mu\nu}$ is the energy-momentum tensor. The Ricci tensor and Ricci scalar are written as

$$R_{\mu\nu} = \frac{\partial \Gamma^\rho_{\mu\nu}}{\partial x^\rho} - \frac{\partial \Gamma^\rho_{\mu\rho}}{\partial x^\nu} + \Gamma^\rho_{\mu\nu} \Gamma^\sigma_{\rho\sigma} - \Gamma^\rho_{\mu\sigma} \Gamma^\sigma_{\nu\rho} \tag{2.3}$$

and

$$R = g^{\mu\nu} R_{\mu\nu}, \tag{2.4}$$

respectively. Here, $\Gamma^{\mu}_{\rho\sigma}$ is the Christoffel symbol, where

$$\Gamma^{\mu}_{\rho\sigma} = g^{\mu\nu}(\frac{\partial g_{\sigma\nu}}{\partial x^{\rho}} + \frac{\partial g_{\rho\nu}}{\partial x^{\sigma}} - \frac{\partial g_{\rho\sigma}}{\partial x^{\nu}}). \tag{2.5}$$

When a gravitational wave is regarded as a perturbation of the Minkowski space, the metric tensor can be written as

$$g_{\mu\nu} = \eta_{\mu\nu} + h_{\mu\nu}. \tag{2.6}$$

Here, h is the term representing the gravitational wave, where $\mid h_{\mu\nu} \mid \ll 1$, and $\eta_{\mu\nu}$ is the Minkowski space, defined as

$$\eta_{\mu\nu} = \begin{pmatrix} -1 & 0 & 0 & 0 \\ 0 & 1 & 0 & 0 \\ 0 & 0 & 1 & 0 \\ 0 & 0 & 0 & 1 \end{pmatrix}. \tag{2.7}$$

Using Eq. (2.6), the Einstein equation in vacuum gives the wave equation in terms of $h_{\mu\nu}$:

$$\Box h_{\mu\nu} = 0, \tag{2.8}$$

$$\Box = \nabla^2 - \frac{1}{c^2}\frac{\partial^2}{\partial t^2}, \tag{2.9}$$

where $\Box$ is called the d'Alembertian. The derivation of Eq. (2.8) is given in Refs. [1, 28, 29] and in many theses on this field. Wave solutions of this equation indicate the existence of gravitational waves. By applying the condition of the transverse-traceless gauge to Eq. (2.8), a gravitational wave propagating in the Z direction is expressed as

$$h_{\mu\nu} = \begin{pmatrix} 0 & 0 & 0 & 0 \\ 0 & h_{+} & h_{\times} & 0 \\ 0 & h_{\times} & -h_{+} & 0 \\ 0 & 0 & 0 & 0 \end{pmatrix} \tag{2.10}$$

This result implies that h_{+} and $h_{\times}$ are polarizations of the gravitational wave.

2.2 Detection using interferometer

2.2.1 Michelson interferometer

The Michelson interferometer is one of the most well-known configurations of GW detectors. This interferometer can be used to directly observe the change in space-time caused by GWs by detecting the amplitude of the interference fringe. Figure 2.1 shows a schematic diagram of the Michelson interferometer. The incident laser beam is divided by a beam splitter (BS). After reflection by the end mirrors, the lasers interfere at the BS. If the arm lengths, l_1 and l_2, are differentially changed then the interference fringe at the point of detection changes. The impinging gravitational wave given by h_+ in Eq. (2.10) causes the differential change in the lengths of the two arms with the right angle.

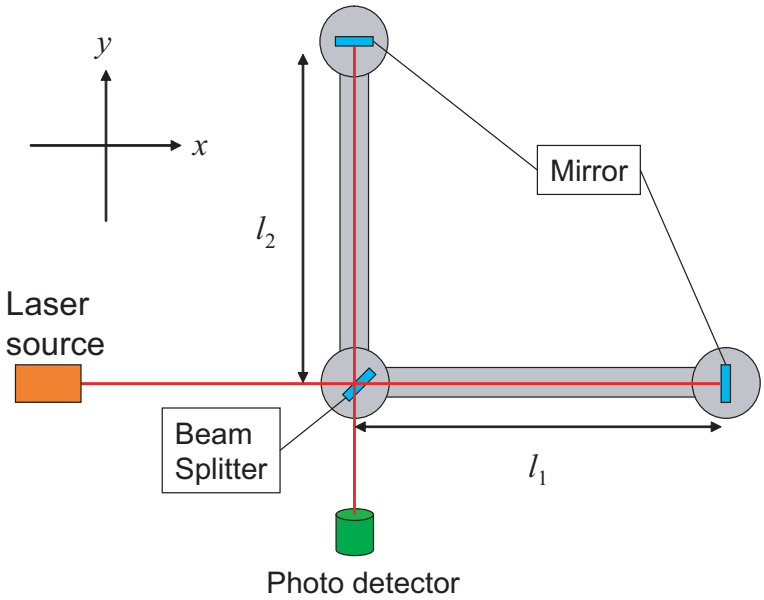

Figure 2.1: Michelson interferometer.

2.2.2 Response of Michelson interferometer

A change in space-time causes a phase shift of the laser. Let us consider that a gravitational wave given by h_+ in Eq. (2.10) enters the Michelson interferometer. A photon in the x direction passes a line element given by

$$ds^2 = -c^2dt^2 + \{1 + h(t)\}dx^2 = 0. \tag{2.11}$$

Then,

$$\{1 - \frac{1}{2}h(t)\}cdt = dx. \tag{2.12}$$

Here, $h(t) \ll 1$ and $\frac{dx}{dt} > 0$ are used. When δt_1 is defined as the round-trip time of a photon between the BS and the end mirror, the integration of Eq. (2.12) gives

$$\int_{t-\delta t_1}^{t} \{1 - \frac{1}{2}h(t')\}cdt' = \frac{2l_1}{c}. \tag{2.13}$$

δt_1 is obtained as

$$\delta t_1 = \frac{2l_1}{c} + \frac{1}{2}\int_{t-\delta t_1}^{t} h(t')dt' \tag{2.14}$$

$$\simeq \frac{2l_1}{c} + \frac{1}{2}\int_{t-\frac{2l_1}{c}}^{t} h(t')dt'. \tag{2.15}$$

Here, the approximation $\delta t_1 \simeq \frac{2l_1}{c}$ is used because $h(t) \ll 1$. The phase shift of the light after one round trip is

$$\phi_1 = \Omega\delta t_1 \tag{2.16}$$

$$= \Omega\left(\frac{2l_1}{c} + \frac{1}{2}\int_{t-\frac{2l_1}{c}}^{t} h(t')dt'\right), \tag{2.17}$$

where the angular frequency of the laser is defined as Ω. Taking the differential change in space-time into account, the phase shift of the arm in the y direction is

$$\phi_2 = \Omega\left(\frac{2l_2}{c} - \frac{1}{2}\int_{t-\frac{2l_2}{c}}^{t} h(t')dt'\right). \tag{2.18}$$

The phase difference between these two arms, defined as $\phi_- \equiv \phi_1 - \phi_2$, is calculated as

$$\phi_- = \frac{2l_-\Omega}{c} + \Omega\int_{t-\frac{2l}{c}}^{t} h(t')dt'. \tag{2.19}$$

Here, $l_1 \simeq l_2 \simeq l$ and $l_- = l_1 - l_2$ are used. By substituting the Fourier transformation of $h(t)$ for the second term of Eq. (2.19), we obtain

$$\phi_- = \int_{-\infty}^{\infty} \frac{2\Omega}{\omega} \sin\left(\frac{l\omega}{c}\right) e^{-i\frac{l\omega}{c}}(\omega) e^{i\omega t} d\omega, \tag{2.20}$$

with $l_- = 0$. Therefore, the response of the Michelson interferometer is given by

$$H_{\mathrm{MI}}(\omega) = \frac{2\Omega}{\omega} \sin\left(\frac{l\omega}{c}\right) e^{-i\frac{l\omega}{c}}. \tag{2.21}$$

This means that the sensitivity of the Michelson interferometer depends on the frequency of GWs. The best sensitivity is obtained when the relation

$$\frac{l\omega}{c} = \frac{\pi}{2} \tag{2.22}$$

is satisfied. The optimal length, l, is about 750 km for a GW of 100 Hz. This is not a realistic value from a practical viewpoint. This is why, a Fabry-Perot (FP) cavity is utilized in current GW detectors to extend the light path length with a realistic baseline.

2.3 Main disturbances in interferometer

There are many different sources of noise in GW detectors. In this section, the main disturbances that may limit the sensitivity in the observation band (10 Hz - 1 kHz) are described. These disturbances determine the design sensitivity in current GW detectors.

2.3.1 Seismic noise

The ground is subjected to continuous seismic vibrations. Seismic vibrations can be modeled as

$$\sqrt{G_{\mathrm{Seis}}} = \frac{\beta}{f^2} \quad [\mathrm{m}/\sqrt{\mathrm{Hz}}], \quad (f > 0.1\,\mathrm{Hz}) \tag{2.23}$$

where β is $10^{-7}\,\mathrm{m\,Hz}^{3/2}$ in an urban area such as the TAMA site and $10^{-9}\,\mathrm{m\,Hz}^{3/2}$ in Kamioka mine, where CLIO is located [30, 31]. The amount of vibration

depends on the weather and the existence and condition of sea waves. The mirror (test mass) is intended to be isolated from the seismic vibrations by multiple suspensions. This seismic noise dominates the sensitivity in the low-frequency region. The isolation ratio resulting from the suspensions is better when the frequency is higher.

2.3.2 Thermal noise

Even thermal fluctuation is a matter of concern for GW detectors despite its small quantity. GW detectors consist of mirrors suspended by pendulums to bring them close to the state of free mass. Therefore, thermal noise can be classified into two categories. One is mirror thermal noise, which is caused by the mirror substrate and coating. The noise spectra for CLIO are estimated in Chapter 4. The other is pendulum thermal noise, which is the main theme of this thesis and is described in detail in Chapters 3 and 5. These two classes of thermal noise are both estimated using the FDT (see Chapter 3).

2.3.3 Shot noise

Shot noise is caused by the fluctuation of the number of photons received by a photodetector (PD). The sensitivity of GW detectors is affected by shot noise in the high-frequency region. The shot noise of a PD is given by [32]

$$\sqrt{G_{\rm Shot}(f)} = l_{\rm c} \times \sqrt{\frac{\hbar\lambda[1+(\tau_{\rm s}\omega)^2]}{4\pi c P_{\rm i}\tau_{\rm s}^2}}, \tag{2.24}$$

where

$$\tau_{\rm s} = \frac{2l_{\rm c}\mathcal{F}}{\pi c} = \frac{2l_{\rm c}}{c}\frac{\sqrt{r_1 r_2}}{1-r_1 r_2}. \tag{2.25}$$

Here, $\sqrt{G_{\rm Shot}}$ is the one-sided power spectrum density corresponding to the mirror displacement noise, which includes the signal to noise ratio. $l_{\rm c}$ is the length of the FP cavity, $\hbar$ is the reduced Planck's constant, λ is the wavelength of the laser, c is the light velocity, η is the quantum efficiency of the PD, $P_{\rm i}$ is the power of laser incident to the FP cavity, and $\mathcal{F}$ is the

finesse of the cavity defind as $\pi\sqrt{r_1 r_2}/(1 - r_1 r_2)$, where, two mirrors of the FP cavity have each reflectance of r_1 and r_2 for an electric field. To reduce shot noise, a high-power laser is required.

2.4 Gravitational wave detectors

2.4.1 Japanese interferometers

There are two interferometric GW detectors in Japan, CLIO and TAMA300. As a future project, LCGT is being studied and its precise design is in progress. Some of the work carried out at CLIO and TAMA300 is related to the development of the fundamental technology for LCGT.

- CLIO

The experiments in this thesis were performed at CLIO (Cryogenic Laser Interferometer Observatory). CLIO is located in the Kamioka facility, which is 220 km away from Tokyo and located 1000 m underground, where there is little seismic noise. The CLIO interferometer has a baseline of 100 m. The main goal of CLIO is to reduce mirror thermal noise by cooling the mirrors, Details of which are described in Chapter 4. The same cooling technique is to be applied to LCGT. The underground site and cooling technique are unique features of CLIO.

- TAMA300

TAMA300 is located in the city of Mitaka, near Tokyo. The baseline is 300 m. Its configuration is power-recycled FP Michelson interferometer. As the elemental technology for LCGT, a seismic attenuation system (SAS, called TAMA-SAS) [9, 33, 34, 35] has been installed and studied in recent works. The study of the variable-bandwidth technique (known as resonant sideband extraction) is in progress.

- LCGT

LCGT (Large-scale Cryogenic Gravitational-wave Telescope) [14] is also planned to be located in Kamioka mine. The goal of LCGT is the first detection of a GW. Its baseline is 3 km. The seismic noise is reduced by the SAS and by the quiet location of Kamioka mine. Thermal noise is suppressed by cooling mirrors and suspensions. Shot noise is lowered using a high-power 75 W laser (at the BS). The variable-bandwidth technique is utilized.

2.4.2 Interferometers abroad

After a competition for the first detection of a GW, the worldwide cooperation is necessary to carry out the all-sky observation of GWs.

- LIGO

LIGO (Laser Interferometer Gravitational Wave Observatory) [3] is a project of the United States of America. It contains two interferometers with a 4 km baseline and one with a 2 km baseline. LIGO has the world's highest sensitivity of around 100 Hz.

- VIRGO

VIRGO (named after the Virgo cluster) [4] is a project of Italy and France. Its baseline is 3 km. VIRGO has a super-attenuator (SA) [36, 37], which is a high-performance seismic isolator. TAMA-SAS is based on the SA.

- GEO600

GEO600 [5] is a project of Germany and the United Kingdom. Its baseline is 600 m. GEO has a signal recycling technique, which is another variable-bandwidth method.

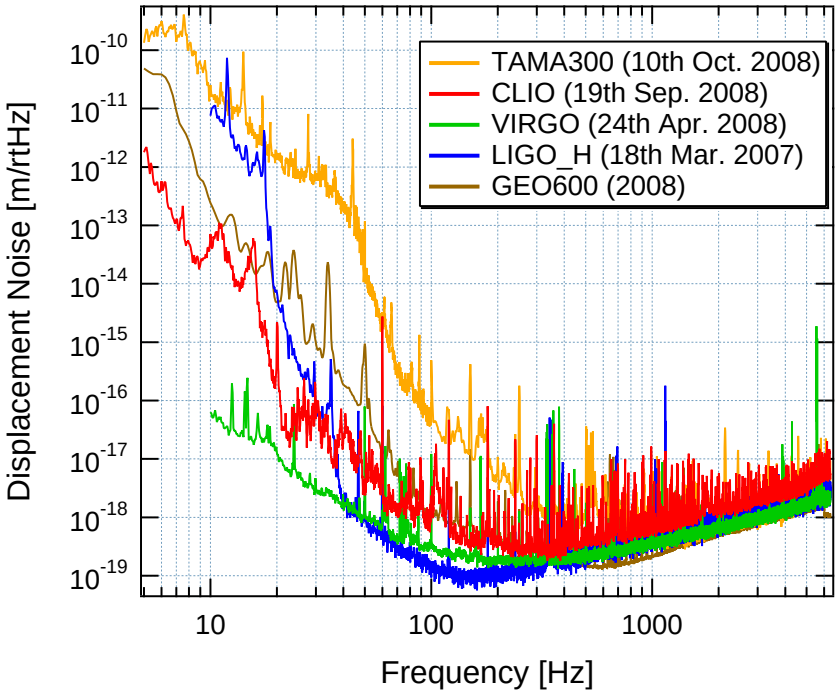

Figure 2.2: Comparison of sensitivities of GW detectors around the world.

2.4.3 Comparison of sensitivities around the world

Figure 2.2 shows the sensitivities of current GW detectors around the world. Note that these sensitivities are the displacement noise of the interferometers. The displacement noise, D_S, and strain sensitivity, h, are related by

$$h = \frac{D_S}{L}, \tag{2.26}$$

where L is the baseline of the interferometer. Hence, an interferometer with a longer baseline has a higher sensitivity to GWs. The level of the displacement noise of CLIO, described in section 5.3, is now comparable with that of other interferometers [38] around the world. In particular, the noise level is lower than that of LIGO below 30 Hz owing to the use of the Kamioka site and multiple suspensions.

Chapter 3

Thermal fluctuation of pendulum

The thermal fluctuation is calculated using the FDT [17, 18]. The FDT indicates that the existence of energy loss (dissipation) causes the fluctuation to the dissipated object. In this chapter, we review useful equations based on this theory and its application to a pendulum subjected to dissipation mechanisms [19, 39].

3.1 Fluctuation-dissipation theorem

A number of expressions can be used to describe a mechanical response. The transfer function from the force applied to an observed object, F, to a displacement, x, of an observed object in the frequency domain is defined as

$$H(\omega) \equiv \frac{\tilde{x}(\omega)}{\tilde{F}(\omega)}. \tag{3.1}$$

Also, the mechanical impedance is given by

$$Z(\omega) \equiv \frac{\tilde{F}(\omega)}{i\omega\tilde{x}(\omega)} \tag{3.2}$$

$$= \frac{1}{i\omega H(\omega)}. \tag{3.3}$$

There are other response functions. The mechanical resistance is

$$R(\omega) \equiv \mathrm{Re}[Z(\omega)], \tag{3.4}$$

the mechanical admittance is

$$Y(\omega) \equiv 1/Z(\omega), \tag{3.5}$$

and the mechanical conductance is

$$\sigma(\omega) \equiv \mathrm{Re}[Y(\omega)]. \tag{3.6}$$

Using the formula for mechanical conductance, the fluctuation, G_x (the one-sided power spectrum of x), is expressed by the FDT as

$$G_x(f) = \frac{4k_B T\sigma(\omega)}{\omega^2}, \tag{3.7}$$

where $\omega = 2\pi f$, f is the frequency, k_B is the Boltzmann constant, and T is the temperature. This is called the first FDT. From the relations $\mathrm{Re}[Z] = (Z + Z^*)/2$ and $\mathrm{Im}[Z] = (Z - Z^*)/(2i)$, the conductance, σ, can be expressed as $-\omega\,\mathrm{Im}[H]$. Thus, Eq. (3.7) is rewritten as

$$G_x(f) = -\frac{4k_B T\mathrm{Im}[H]}{\omega}. \tag{3.8}$$

The mechanical conductance and the imaginary part of the transfer function represent the mechanical dissipation. Furthermore, the thermal driving force (fluctuating force) is given by

$$G_f(f) = 4k_B T R(\omega). \tag{3.9}$$

This is called the second FDT, which agrees with the Nyquist relation [40] of

$$< V^2 >= 4k_B T R\,\Delta f. \tag{3.10}$$

Here, V is the thermal electromotive force due to the resistance, R, in a circuit, and Δf the band width. The second FDT is consistent with the

first FDT. The thermal driving force given by Eq. (3.9) is transmitted by the transfer function as

$$G_x(f) = G_f(f) \mid H(\omega) \mid^2 \tag{3.11}$$

$$= \frac{4k_BT}{\omega^2} \frac{\mathrm{Re}[Z(\omega)]}{\mid Z(\omega) \mid^2} \tag{3.12}$$

$$= \frac{4k_BT}{\omega^2} \mathrm{Re}\left[\frac{1}{Z(\omega)}\right] \tag{3.13}$$

$$= \frac{4k_BT\sigma(\omega)}{\omega^2}. \tag{3.14}$$

The final expression is the first FDT.

3.2 Application of the FDT to a pendulum

3.2.1 Harmonic oscillator

The equation of motion of a harmonic oscillator is given as

$$m\ddot{x} + Kx = F(t). \tag{3.15}$$

Here, m is mass of the oscillator, x is the displacement, K is the spring constant, and F is the force applied to the oscillator. The Fourier transformation of Eq. (3.15) can be expressed as

$$-m\omega^2\tilde{x} + m\omega_0^2[1 + i\phi(\omega)]\tilde{x} = \tilde{F}, \tag{3.16}$$

where the spring constant can be considered by including its complex part as

$$K \equiv k(1 + i\phi). \tag{3.17}$$

Here, k is the real part of the spring constant, ϕ is the loss angle, which represents dissipation. The resonant frequency, ω_0, of the oscillator has the relation $k = m\omega_0^2$. From Eq. (3.16) and Eq. (3.2), the mechanical impedance

$$Z(\omega) = \frac{-m\omega^2 + m\omega_0^2[1 + i\phi(\omega)]}{i\omega} \tag{3.18}$$

is obtained. By applying the first FDT to Eq. (3.18), the thermal fluctuation is derived as [19]

$$G_x(f) = \frac{4k_BT}{m\omega}\frac{\omega_0^2\phi(\omega)}{(\omega^2-\omega_0^2)^2+\omega_0^4\phi^2(\omega)}. \tag{3.19}$$

This is the thermal fluctuation of a harmonic oscillator (or a pendulum).

3.2.2 Two-mode oscillator

In GW detectors, multistage pendulums are used to suspend mirrors. The simplest example of a multistage pendulum is a double pendulum, which is modeled as a two-mode oscillator. The equations of motion of the intermediate mass and final (test) mass are written as

$$M_1\ddot{x}_1 + K_1x_1 - K_2(x_2-x_1) = 0, \tag{3.20}$$

$$M_2\ddot{x}_2 + K_2(x_2-x_1) = F(t). \tag{3.21}$$

Here, the subscripts 1 and 2 denote the intermediate mass and final mass, respectively. For instance, K_1 indicates the spring constant of the first-stage pendulum. By substituting $K_j = m_j\omega_j^2(1+i\phi_j)\,;j=1,\,2$ for K_1 and K_2, the above equations are rewritten as

$$M_1[-\omega^2+\omega_1^2(1+i\phi_1)]\tilde{x}_1 - M_2\omega_2^2(1+i\phi_2)(\tilde{x}_2-\tilde{x}_1) = 0, \tag{3.22}$$

$$-M_2\omega^2\tilde{x}_2 + M_2\omega_2^2(1+i\phi_2)(\tilde{x}_2-\tilde{x}_1) = \tilde{F}. \tag{3.23}$$

The mechanical impedance of the final mass can be calculated using the above equations.

$$\begin{aligned} Z(\omega) &= \frac{\tilde{F}}{i\omega\tilde{x}_2} \\ &= \frac{-M_2\omega^2+M_2\omega_2^2(1+i\phi_2)}{i\omega} \\ &\quad - \frac{M_2^2\omega_2^4(1+i\phi_2)^2}{i\omega[-M_1\omega^2+M_1\omega_1^2(1+i\phi_1)+M_2\omega_2^2(1+i\phi_2)]} \end{aligned} \tag{3.24}$$

$$\approx \frac{-M_2\omega^2+M_2\omega_2^2(1+i\phi_2)}{i\omega}. \qquad (\omega \gg \omega_0) \tag{3.25}$$

The second term of Eq. (3.24) is neglected in the case of $\omega \gg \omega_0$. Equation (3.25) only contains the subscript 2 and agrees with Eq. (3.18), which means that the thermal fluctuation of the final mass suspended by a multi-stage pendulum can be calculated using only the final-stage pendulum.

3.3 Dilution factor

A pendulum consists of a mass and suspensions. There is a fixed relationship between the loss angle of the pendulum, $\phi_{\rm p}$, and that of the suspension wires, $\phi_{\rm w}$. According to Ref. [19],

$$\phi_{\rm p} = \phi_{\rm w} \frac{E_{\rm el}}{E_{\rm grav} + E_{\rm el}} \approx \phi_{\rm w} \frac{E_{\rm el}}{E_{\rm grav}}, \tag{3.26}$$

where $E_{\rm el}$ and $E_{\rm grav}$ represent the energy stored in the flexing wire and in the gravitational field, respectively. Using the fact that $E_{\rm el}/E_{\rm grav} = k_{\rm el}/k_{\rm grav}$, the relationship between $\phi_{\rm p}$ and $\phi_{\rm w}$ can be evaluated. The spring constant of the pendulum has been found to be $k_{\rm grav} = mg/l$ for a pendulum of length l. The elastic spring constant of n wires is $k_{\rm el} = n\sqrt{TEI}/(2l^2)$. Here, T is the tension per wire, E is the Young's modulus, and I is the moment of inertia of the wire cross section. Therefore, Eq. (3.26) is rewritten as

$$\phi_{\rm p} = \phi_{\rm w} D_{\rm dil}, \tag{3.27}$$

where $D_{\rm dil}$ is defined as

$$D_{\rm dil} \equiv \frac{n\sqrt{TEI}}{2mgl}. \tag{3.28}$$

The term $D_{\rm dil}$ is called the dilution factor because the dissipation of the wire is diluted.

3.4 Classification of types of dissipation

3.4.1 Viscous damping

Viscous damping is the most familiar damping mechanism and is also called velocity damping. This damping is caused by a resistance force that is pro-

portional to the velocity. For example, air resistance, eddy currents, and the viscous resistance of a liquid are subjected to this damping mechanism. The equation of motion of a harmonic oscillator with viscous damping is

$$m\ddot{x} + \Gamma\dot{x} + m\omega_0^2 x = F(t). \tag{3.29}$$

Here, Γ is the damping coefficient (constant). By applying a Fourier transformation, Eq. (3.29) can be rewritten as

$$(-m\omega^2 + m\omega_0^2 + i\Gamma\omega)\tilde{x} = \tilde{F}. \tag{3.30}$$

The comparison with Eq. (3.16) gives

$$\Gamma = \frac{m\omega_0^2\phi}{\omega}. \tag{3.31}$$

From the Q-factor definition (see Appendix A) of

$$Q = \frac{1}{\phi(\omega_0)}, \tag{3.32}$$

the relation between Γ and the Q-factor can be derived as

$$\Gamma = \frac{m\omega_0}{Q}. \tag{3.33}$$

Also, by comparing Eq. (3.33) with Eq. (3.31), the relation between the loss angle, $\phi(\omega)$, and the Q-factor is

$$\phi(\omega) = \frac{\omega}{\omega_0 Q}. \tag{3.34}$$

This frequency dependence of the dissipation characterizes the viscous damping.

Thus, by substituting Eq. (3.34) into Eq. (3.19), the thermal fluctuation of a pendulum due to viscous damping [19] is

$$G_x(f) = \frac{4k_BT}{mQ\omega}\frac{\omega_0^2}{(\omega^2 - \omega_0^2)^2 + \omega_0^4/Q^2}. \tag{3.35}$$

Approximate expressions for $G_x(f)$ in the lower-frequency and higher-frequency regions are respectively given by

$$G_x(f) = \frac{4k_BT}{m\omega_0^3 Q} = \text{const.} \qquad (\omega \ll \omega_0) \tag{3.36}$$

$$G_x(f) = \frac{4k_BT\omega_0}{mQ}\frac{1}{\omega^4} \propto f^{-4}. \qquad (\omega \gg \omega_0) \tag{3.37}$$

When we compare the thermal fluctuation with the sensitivity (the displacement noise) of GW detectors, $\sqrt{G}$ is employed. Hence,

$$\sqrt{G_x(f)} \propto \begin{cases} \text{const.} & (\omega \ll \omega_0) \\ f^{-2}. & (\omega \gg \omega_0) \end{cases} \tag{3.38}$$

It has been shown that the thermal noise of a pendulum due to viscous damping is inversely proportional to the square of the frequency in the high-frequency region, which is the observation band of GW detectors.

3.4.2 Structure damping

Structure (structural) damping is a type of internal loss that is also called the intrinsic loss. The characteristic of this type of dissipation is its independence of frequency, and it is represented as

$$\phi(\omega) = \frac{1}{Q} = \text{const.} \tag{3.39}$$

Then, using Eq. (3.19), the thermal fluctuation of a pendulum due to structure damping [19] is

$$G_x(f) = \frac{4k_BT}{mQ\omega}\frac{\omega_0^2}{(\omega^2-\omega_0^2)^2+\omega_0^4/Q^2}. \tag{3.40}$$

Approximate expressions for $G_x(f)$ in the lower-frequency and higher-frequency regions are

$$G_x(f) = \frac{4k_BT}{m\omega_0^2 Q}\frac{1}{\omega} \propto f^{-1} \qquad (\omega \ll \omega_0) \tag{3.41}$$

$$G_x(f) = \frac{4k_BT\omega_0^2}{mQ}\frac{1}{\omega^5} \propto f^{-5}, \qquad (\omega \gg \omega_0) \tag{3.42}$$

and

$$\sqrt{G_x(f)} \propto \begin{cases} f^{-1/2} & (\omega \ll \omega_0) \\ f^{-5/2}. & (\omega \gg \omega_0) \end{cases} \tag{3.43}$$

It is worth emphasizing that the thermal noise of a pendulum due to structure damping is inversely proportional to the frequency raised to the power of 2.5 in the high-frequency region, in contrast to the frequency dependence of viscous damping. This difference originates from Eq. (3.34) and Eq. (3.39).

3.4.3 Thermoelastic damping

Thermoelastic damping is caused by thermal expansion. A local deformation gives rise to a thermal gradient, which causes a force to act against the deformation. The thermal diffusion of a material determines its response to an expansion force. According to Ref. [19], the loss angle, $\phi(\omega)$, is given by

$$\phi(\omega) = \Delta \frac{\omega\tau_{\mathrm{r}}}{1 + (\omega\tau_{\mathrm{r}})^2}, \tag{3.44}$$

where Δ is the relaxation strength and τ_{r} is the relaxation time. Δ is determined by

$$\Delta = \frac{E\alpha_{\mathrm{E}}^2 T}{\rho C}. \tag{3.45}$$

Here, E is the Young's modulus, α_{E} is the thermal expansion coefficient, T is the temperature, ρ is the density of the material, and C is the specific heat per unit mass. Note that this type of dissipation depends on the temperature. The relaxation time, τ_{r}, characterizes the property of this type of dissipation. In the case of a cylindrical wire, the characteristic frequency, f_{r}, is

$$f_{\mathrm{r}} = \frac{1}{2\pi\tau_{\mathrm{r}}} = 2.16\frac{D}{d^2}, \tag{3.46}$$

where d is the diameter of the wire and D is the thermal diffusion coefficient, given by

$$D = \frac{\kappa}{\rho C}. \tag{3.47}$$

Here, κ is the thermal conductivity.

Using Eq. (3.19), Eq. (3.44), Eq. (3.45), and Eq. (3.28), the thermal fluctuation of a pendulum due to structure damping is written as

$$G_x(f) = \frac{4k_BT}{m\omega} \frac{\omega_0^2 \left(\Delta \frac{\omega\tau_\mathrm{r}}{1+(\omega\tau_\mathrm{r})^2} D_\mathrm{dil} \right)}{(\omega^2-\omega_0^2)^2 + \omega_0^4 \left(\Delta \frac{\omega\tau_\mathrm{r}}{1+(\omega\tau_\mathrm{r})^2} D_\mathrm{dil} \right)^2} \tag{3.48}$$

$$\approx \frac{4k_BT^2\omega_0^2}{m\omega^5} \frac{E\alpha_\mathrm{E}^2}{\rho C} \frac{f/f_\mathrm{r}}{1+(f/f_\mathrm{r})^2} D_\mathrm{dil}. \qquad (\omega \gg \omega_0) \tag{3.49}$$

The final term is approximated when $\omega \gg \omega_0$ because the observation band is sufficiently larger than the pendulum resonance frequency. The slope of the noise spectrum has the following dependence on the characteristic frequency, f_r.

$$\sqrt{G_x(f)} \propto \begin{cases} f^{-2} & (\omega_0 \ll \omega < f_\mathrm{r}) \\ f^{-3}. & (\omega_0 \ll \omega, \text{ and, } f_\mathrm{r} < \omega) \end{cases} \tag{3.50}$$

Chapter 4

Thermal-noise-limited interferometer (CLIO)

4.1 Overview of CLIO

4.1.1 Goal

CLIO [10, 11, 12, 13], is a prototype of the next Japanese gravitational wave (GW) telescope project LCGT [14], featuring the use of cryogenic mirrors and a quiet underground site. The cryogenic technique is important for achieving the target sensitivity of LCGT. However, nobody has ever confirmed the thermal noise reduction resulting from the use of cooling mirrors. The main goal of CLIO is to demonstrate the improvement of sensitivity through the reduction of mirror thermal noise by cooling the sapphire mirrors. Figure 4.1 shows the target sensitivity of CLIO. The design sensitivity is limited by the mirror thermal noise and suspension thermal noise around 100 Hz at room temperature, which will be reduced by cooling.

4.1.2 Initial design sensitivity

The estimates of noise in Fig. 4.1 are only the dominant components. The mirror thermal noise and suspension thermal noise have various sources and

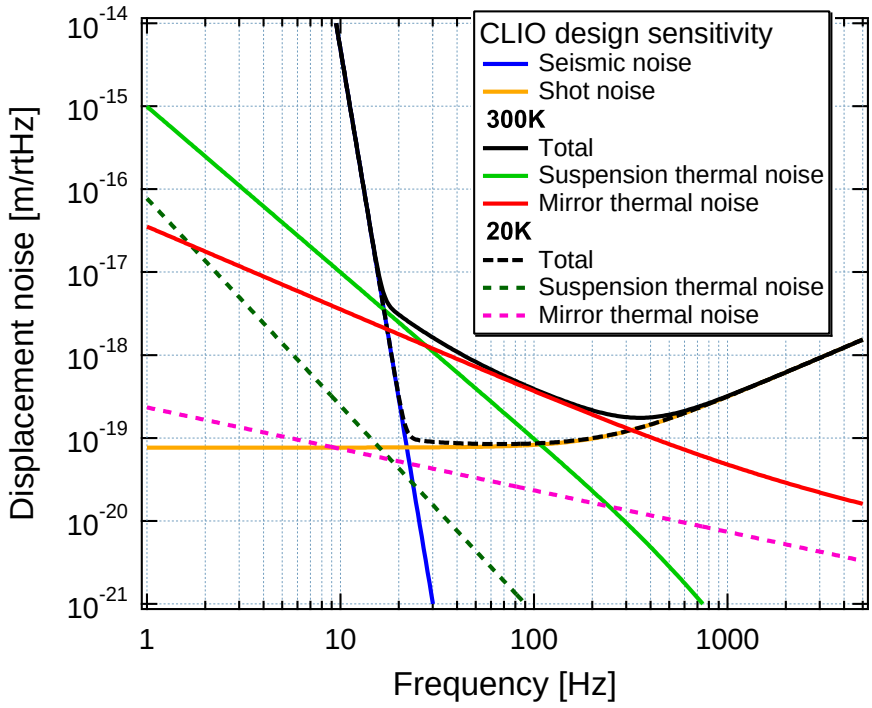

Figure 4.1: Target sensitivity of CLIO.

mechanisms. Figure 4.2 shows the thermal noise generated by the main dissipation mechanisms of the mirrors and suspensions. This is the initial design sensitivity. The mirrors are made of sapphire and are suspended by multistage pendulums with sapphire fibers used in the final stage. The values of parameters used in these estimates are given in Table 4.1 and Table 4.2, which also show the notation used in the following equations.

The seismic noise is calculated from

$$\sqrt{G_{\rm Seis}} = \frac{10^{-9}}{f^2} \times \left(\frac{5}{f}\right)^{12}. \tag{4.1}$$

The term $10^{-9}/f^2$ is used to model the seismic vibration in Kamioka mine. The term $(5/f)^{12}$ is the transfer function of a seismic isolation system with 6-stage pendulums; the resonance frequency is 5 Hz.

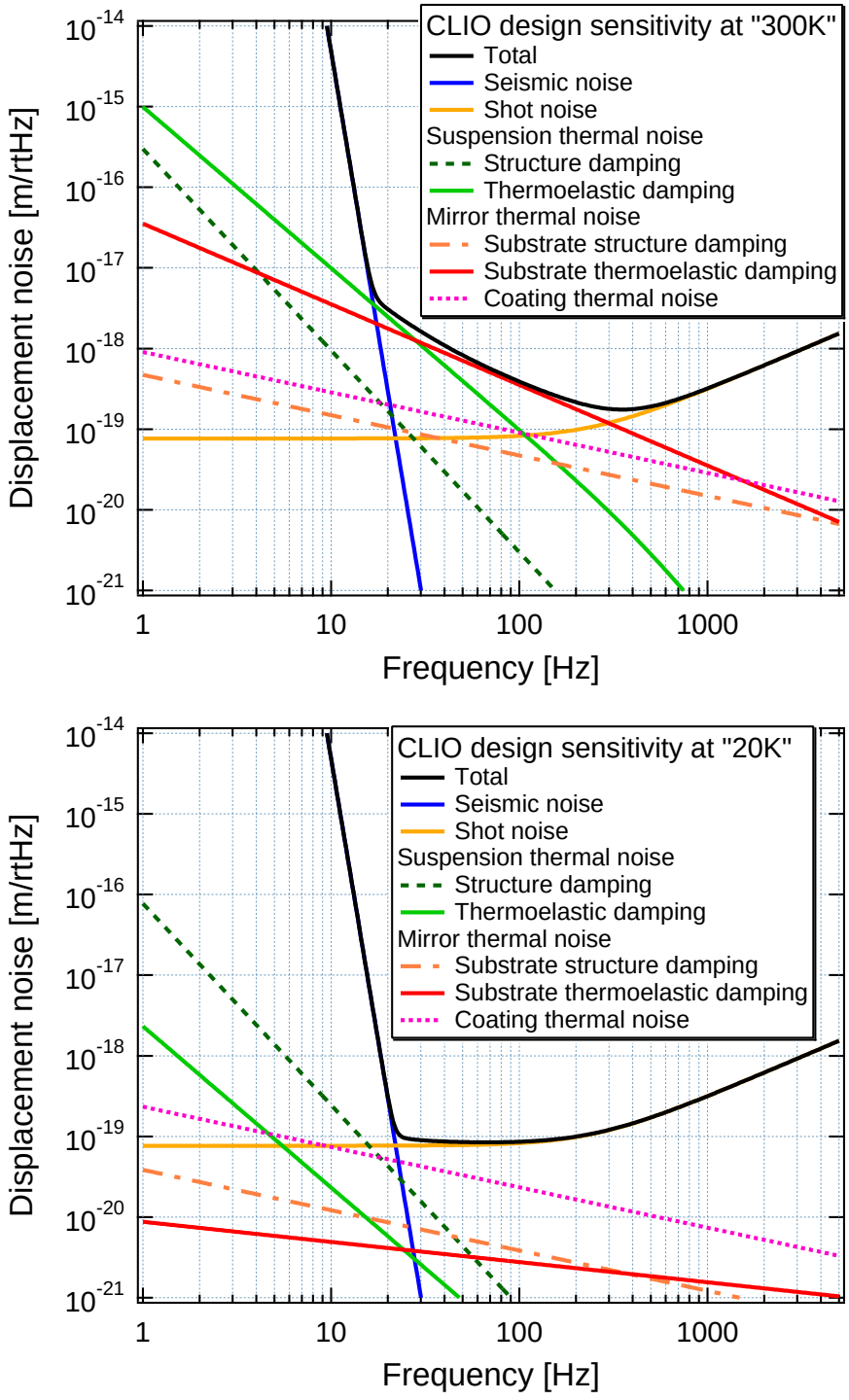

Figure 4.2: Initial design sensitivity of CLIO.

Using Eq. (2.24), the shot noise is estimated from

$$\sqrt{G_{\rm Shot}(f)} = 2l_{\rm c} \times \sqrt{\frac{\hbar\lambda[1+(\tau_{\rm s}\omega)^2]}{4\pi c P_0 \tau_{\rm s}^2}}, \tag{4.2}$$

where

$$\tau_{\rm s} = \frac{2l_{\rm c}\mathcal{F}}{\pi c} = \frac{2l_{\rm c}}{c}\frac{\sqrt{r_1 r_2}}{1-r_1 r_2}. \tag{4.3}$$

Two PDs are used. For simplicity, the quantum efficiency of the PDs is assumed to be unity. The incident laser power at the BS is 0.5 W.

The mirror thermal noise was well identified by Numata et al. [15] and Black et al. [16]. Each mirror consists of a substrate and a reflective coating, which are both noise sources. The substrate has two main dissipation mechanisms. One is structure damping. According to Ref. [15], the noise spectrum resulting from structure damping is given by

$$G_{\rm SB}(f) = \frac{4k_B T}{\omega}\frac{1-\sigma^2}{\sqrt{\pi}Ew_0}\phi_{\rm sub}(f). \tag{4.4}$$

The other is thermoelastic damping, whose noise spectrum is written as

$$G_{\rm ST}(f) = \frac{16}{\sqrt{\pi}}\alpha_{\rm E}^2(1+\sigma)^2\frac{k_B T^2}{\rho^2 C^2}\frac{\kappa}{w_0^3}\frac{1}{\omega^2}\Omega^2 J(\Omega). \tag{4.5}$$

Here, Ω is the normalized frequency characterized by $\Omega = \omega/\omega_{\rm c}$, where $\omega_{\rm c} = 2\kappa/(\rho C w_0^2)$. J is a shape function given by

$$J(\Omega) = \frac{\sqrt{2}}{\pi^{3/2}}\int_0^\infty du \int_{-\infty}^\infty dv \frac{u^3 e^{-u^2/2}}{(u^2+v^2)[(u^2+v^2)^2+\Omega^2]}. \tag{4.6}$$

This function is approximated as

$$J(\Omega) = \begin{cases} \dfrac{1}{2\sqrt{2}\,\Omega^{1/2}} & (\Omega \ll 1) \\ \dfrac{1}{\Omega^2}. & (\Omega \gg 1) \end{cases} \tag{4.7}$$

The Brownian motion of the mirror coating due to structure damping is expressed as

$$G_{\rm CB}(f) = G_{\rm SB}(f)\left(1 + \frac{2}{\sqrt{\pi}}\frac{1-2\sigma}{1-\sigma}\frac{\phi_{\rm coat}}{\phi_{\rm sub}}\frac{d_{\rm coat}}{w_0}\right). \tag{4.8}$$

The coating film consists of multilayered films of SiO_2 and Ta_2O_5. The mirror thermal noise is dominated by the thermoelastic damping of the bulk at room temperature as shown in Fig. 4.2. By cooling the mirrors, the thermoelastic dissipation is reduced, and the mirror-coating noise becomes the primary noise source at 20 K. Cooling the sapphire mirrors and suspensions greatly increases the thermal diffusion coefficient of the mirrors, D (see Table 4.2). The characteristic frequency, $\omega_c/2\pi$ (as $\Omega = 1$), is increased from 0.19 Hz to 7.6×10^4 Hz at the front mirror with the increase in D. Then, J in the observation band is applied to each temperature, where

$$J(\Omega) = \begin{cases} \dfrac{1}{2\sqrt{2}\,\Omega^{1/2}} & (20\,\mathrm{K}) \\ \dfrac{1}{\Omega^2}. & (300\,\mathrm{K}) \end{cases} \tag{4.9}$$

Therefore, the frequency dependence of thermal noise due to thermoelastic damping is also changed from f^{-1} to $f^{-1/4}$ around 100 Hz (the red line in Fig. 4.2). The mirror thermal noise from the thermoelastic damping is independent of the beam radius, w_0, at 20 K.

The suspension thermal noise is calculated using Eq. (3.37), Eq. (3.42), and Eq. (3.49) in the previous chapter. The wires used to suspend the mirrors are assumed to be made of sapphire fibers. Note that sapphire fibers are only used at the final stage of the CLIO experiment because they are expensive and fragile. Other materials (tungsten, Bolfur [41], and aluminum) are used in the commissioning stage. From Fig. 4.2, the primary dissipation mechanism of the suspension thermal noise changes upon cooling the suspensions. The thermal noise due to thermoelastic damping is dominant at room temperature. On the other hand, that due to structure damping is the closest to the target sensitivity at 20 K. The characteristic frequency, f_r, given by Eq. (3.46) is 500 Hz at room temperature and 2×10^8 Hz at 20 K.

Table 4.1: Parameters for the design sensitivity.

Laser, main cavity, and suspension		
Notation	Parameter	Value
λ	Wavelength [m]	1064×10^{-9}
P_0	Laser power at BS [W]	0.5
Main cavity		
l_c	Length [m]	100
$\mathcal{F}$	Finesse	3000
τ_s	Storage time [ms]	0.637
f_cut	Cutoff frequency [Hz]	250
r_1	Reflectance of front mirror	0.9995
r_2	Reflectance of end mirror	0.9995
R_2	Curvature of end mirror [m]	150
w_1	Beam radius at front mirror [mm]	4.89
w_2	Beam radius at end mirror [mm]	8.48
Suspension		
l_sus	Length of final-stage suspension [m]	0.4
d_sus	Diameter of sapphire fiber [m]	250×10^{-6}
N_sus	Number of fibers	4
E_sus	Young's modulus of fiber [Pa]	4.0×10^{11}
f_p	Resonance frequency of pendulum [Hz]	0.788
ϕ_p	Loss angle of final-stage pendulum	1.0×10^{-9}
ϕ_sus	Loss angle of fiber	2×10^{-7}
Q_p	Q-factor of pendulum	9.8×10^{8}
D_dil	Dilution factor	5.1×10^{-3}
f_r20	Characteristic frequency (20 K) [Hz]	2.0×10^{8}
f_r300	Characteristic frequency (300 K) [Hz]	5.0×10^{2}

Table 4.2: Parameters for the design sensitivity.

Sapphire mirror		
Notation	Parameter	Value
ρ	Density [kg/m^3]	4.0×10^3
$r_{\rm m}$	Radius [m]	5×10^{-2}
$h_{\rm m}$	Height [m]	6×10^{-2}
m	Mass [kg]	1.88
$E_{\rm m}$	Young's modulus of mirror [Pa]	4.0×10^{11}
σ	Poisson ratio	0.27
$Q_{\rm m20}$	Q-factor of mirror material (20 K)	10^8
$Q_{\rm m300}$	Q-factor of mirror material (300 K)	10^7
$\alpha_{\rm E20}$	Thermal expansion coefficient (20 K) [1/K]	5.6×10^{-9}
$\alpha_{\rm E300}$	Thermal expansion coefficient (300 K) [1/K]	5.4×10^{-6}
$C_{\rm m20}$	Specific heat (20 K) [J/(kg $\cdot$ K)]	0.69
$C_{\rm m300}$	Specific heat (300 K) [J/(kg $\cdot$ K)]	7.9×10^2
$\kappa_{\rm m20}$	Thermal conductivity (20 K) [W/(m $\cdot$ K)]	1.57×10^4
$\kappa_{\rm m300}$	Thermal conductivity (300 K) [W/(m $\cdot$ K)]	46
$D_{\rm m20}$	Thermal diffusion coefficient (20 K)	5.69
$D_{\rm m300}$	Thermal diffusion coefficient (300 K)	1.46×10^{-5}
$d_{\rm coat}$	Thickness of mirror coating [m]	7.5×10^{-6}
$\phi_{\rm coat}$	Loss angle of mirror coating	4×10^{-4}

4.1.3 Location

CLIO is located in Kamioka mine, which is 220 km away from Tokyo and lies 1000 m underground, below the top of a mountain. LCGT is planned to be constructed in this area. This underground site is suitable for interferometric GW detectors because the seismic noise is about 2 orders less than that in urban areas [30, 31]. This is helpful for achieving the target sensitivity and for obtaining stability. Figure 4.3 shows a schematic view of the Kamioka observatory. The Super-Kamiokande neutrino observatory is also located at this facility.

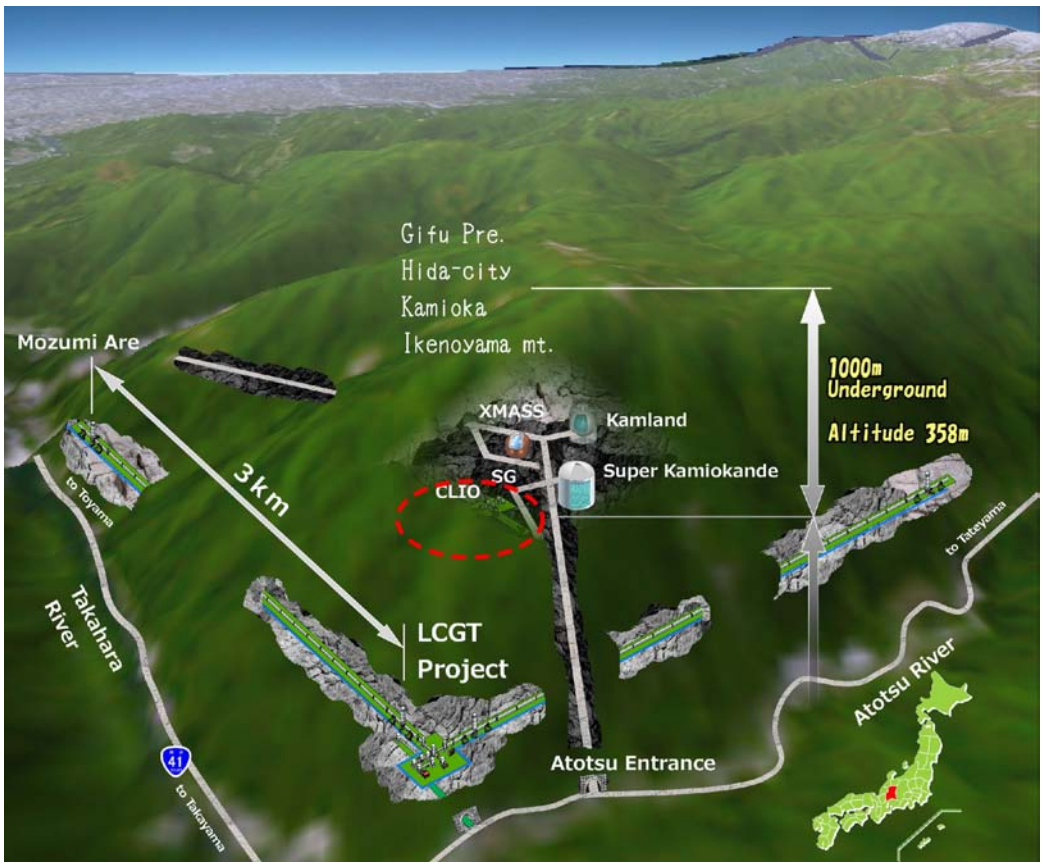

Figure 4.3: Schematic view of Kamioka mine. (The original picture was drawn by Dr. Miyoki)

4.1.4 History

The CLIO project started in 2002. First, tunnels for CLIO were constructed. After the installation of the equipment, a one-arm cavity experiment began in 2005. The CLIO interferometer was fully operated on February 18th, 2006.

Observations with the aim of detecting GWs from the Vela pulsar (PSR J0835-4510) were performed in 2007 [42] since the CLIO "strain" sensitivity of approximately 22 Hz was comparable with those of VIRGO (3 km arm) and LIGO (4 km arm) at that time.

So far, cryogenic systems have been developed [43, 44, 45] and applied to CLIO [46], and cooling mirrors have been realized [47]. All sapphire mirrors were cooled to less than the required temperature of 20 K. However, thermal noise due to a conductive coil holder, which appeared from 20 Hz to 300 Hz with a slope of f^{-2} (f is frequency) prevented the sensitivity from reaching the thermal noise levels of the suspensions and mirrors at both room temperature and 20 K [47]. We were able to remove the extra thermal noise by noise hunting, as reported in recent works [48], and the design sensitivity at room temperature was achieved. In the experiments described in this thesis, CLIO was operated at room temperature.

4.2 Configuration

4.2.1 Locked Fabry-Perot style interferometer

Figure 4.4 shows a schematic view of CLIO. The laser beam used (InnoLight Mephisto) has a power of 2 W and a 1064 nm wavelength. It is shaped into the TEM00 mode through a mode cleaner (MC) cavity with a length of 9.5 m, and then injected into two 100-m-length FP cavities after being divided by a BS. These cavities are arranged in an L-shape. All of the returned (reflected) beam from each arm cavity is extracted by an optical circulator formed by a $\lambda/4$ plate and a polarized BS. Thus, this configuration employs neither optical recombination by a Michelson interferometer nor

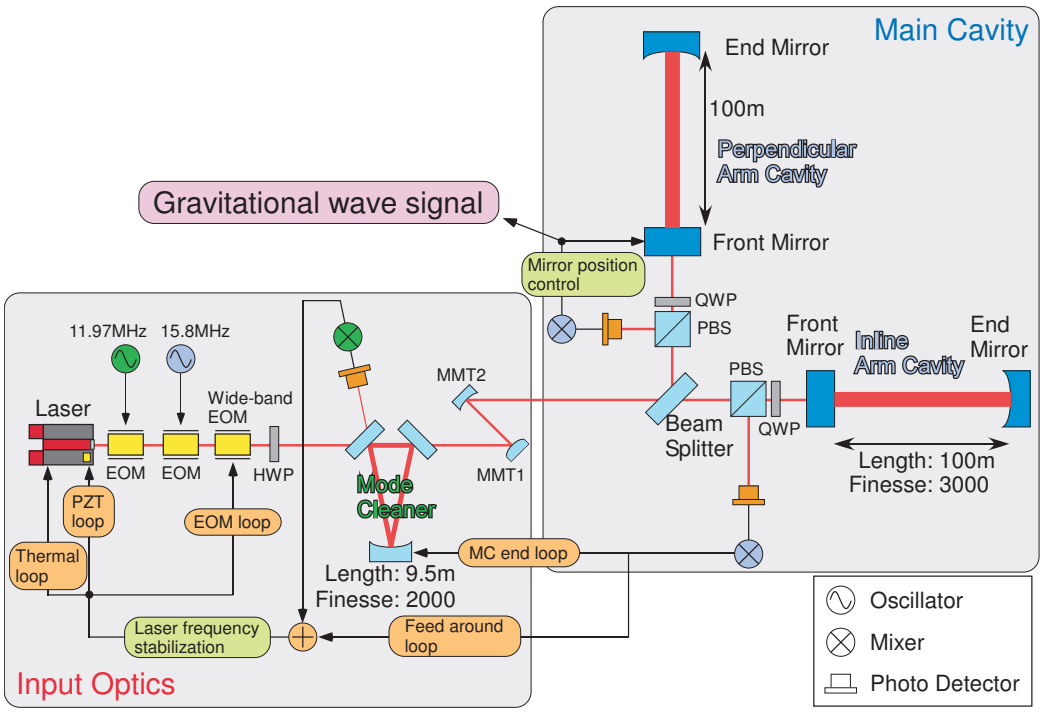

Figure 4.4: Schematic view of CLIO; CLIO is a so-called locked Fabry-Perot interferometer, which has two 100 m FP cavities with a mode cleaner. The optics, lenses, Faraday isolators, and some of the wave plates are omitted in this figure. EOM, electrooptic modulator; HWP, half-wave plate; QWP, quarter-wave plate; MMT, mode-matching telescope; PBS, polarized beam splitter.

optical recycling schemes. The cavities are kept on resonance ("locked") by servo systems. The Pound-Drever-Hall technique [49] is employed as a readout method for the displacement signals of the mirrors. For this purpose, the phase modulations at 15.8 MHz and 11.97 MHz are used for the arm cavities and the MC cavity, respectively. A multistage control system [50] is applied for laser frequency stabilization, which has two cascaded loops of the MC and an arm cavity. The inline arm is locked by controlling the frequency. The perpendicular arm is locked by controlling the mirror. A differential displacement between the two arm cavities, corresponds to GW signals, can

be obtained from the feedback signal to the coil-magnet actuators.

The angular alignments of all mirrors are tuned by movable stages on the suspensions. Coil-magnet actuators are set for the front mirror in the perpendicular cavity only, so as to keep the optical path length of the cavity locked.

4.2.2 Input optics

The layout of the input optics is shown in Fig. 4.5. The laser beam (InnoLight Mephisto) has a nominal power of 2 W and a 1064 nm wavelength. However, the actual output power was 1 W in the experiments described in Chapter 5 because the crystal of the laser had been contaminated by dust in the air. The incident laser power to the MC was 0.23 W immediately before the MC. The two QPDs (Quadrant Photodetectors) in Fig. 4.5 currently only sense the beam position. They can be extended to a wavefront sensor (WFS) [51, 52] to sense the incident laser axis or mirror alignments of the MC.

4.2.3 Mirror suspension

Figure 4.6 shows the suspension system of the four sapphire mirrors in the main cavity. The four mirrors of the two arm cavities are individually suspended by 6-stage pendulums, which include 4-stage blade springs and 2-stage wire suspensions for isolation from seismic vibration. The pendulum has a primary-mode resonance frequency of about 0.5 Hz. The intermediate mass is damped by magnets so as to suppress the resonant motion. The mirrors have weights of 1.9 kg (front) and 1.8 kg (end), and are made of sapphire. The mirrors are cylindrical with diameters of 100 mm (front) and 98 mm (end), and have lengths of 60 mm and 59 mm, respectively. They are suspended by 2-loop wires at the final stage, whose resonance frequency is 0.79 Hz. At room temperature, Bolfur [41] wires are employed to suspend the mirrors.

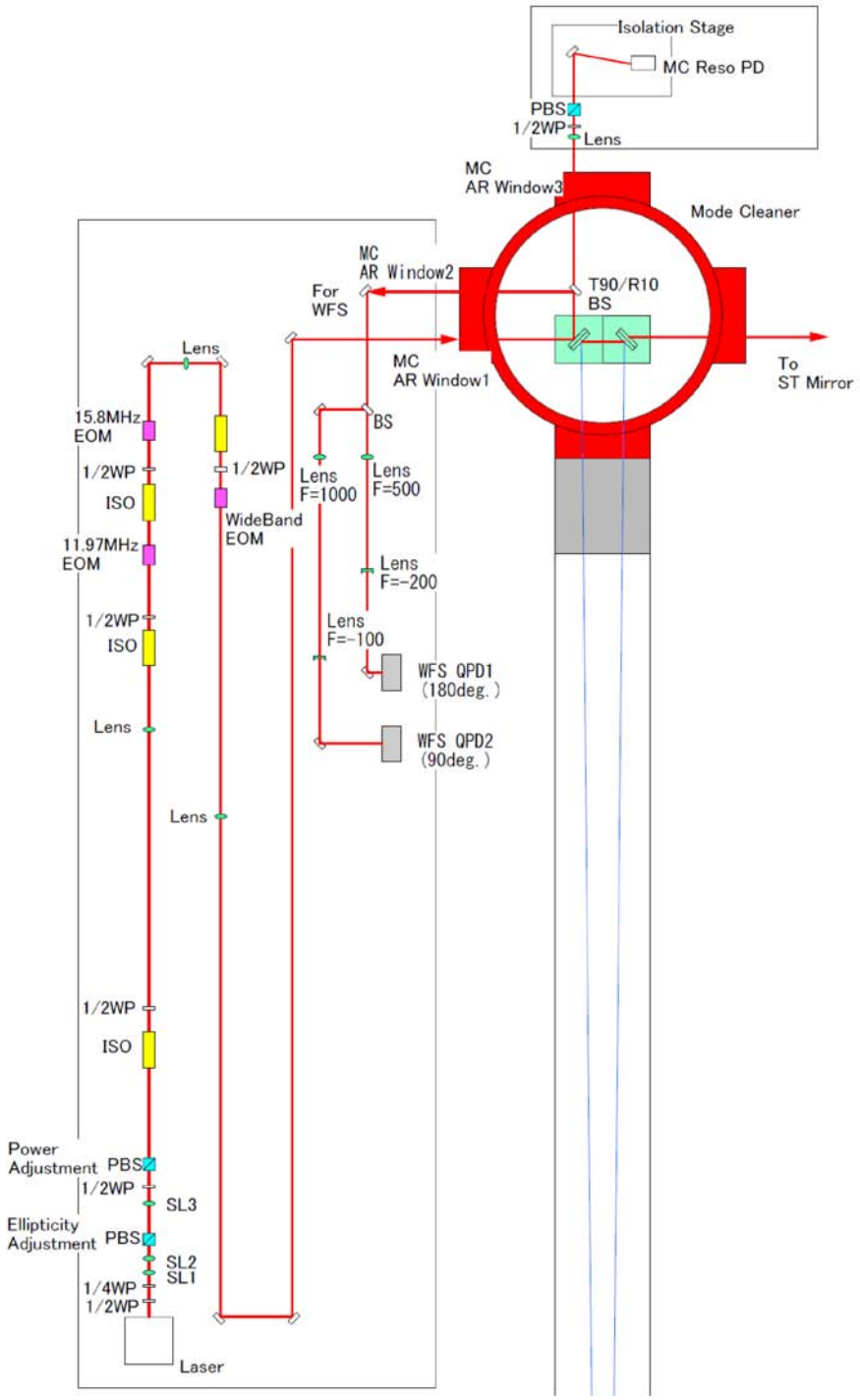

Figure 4.5: Schematic view of input optics.

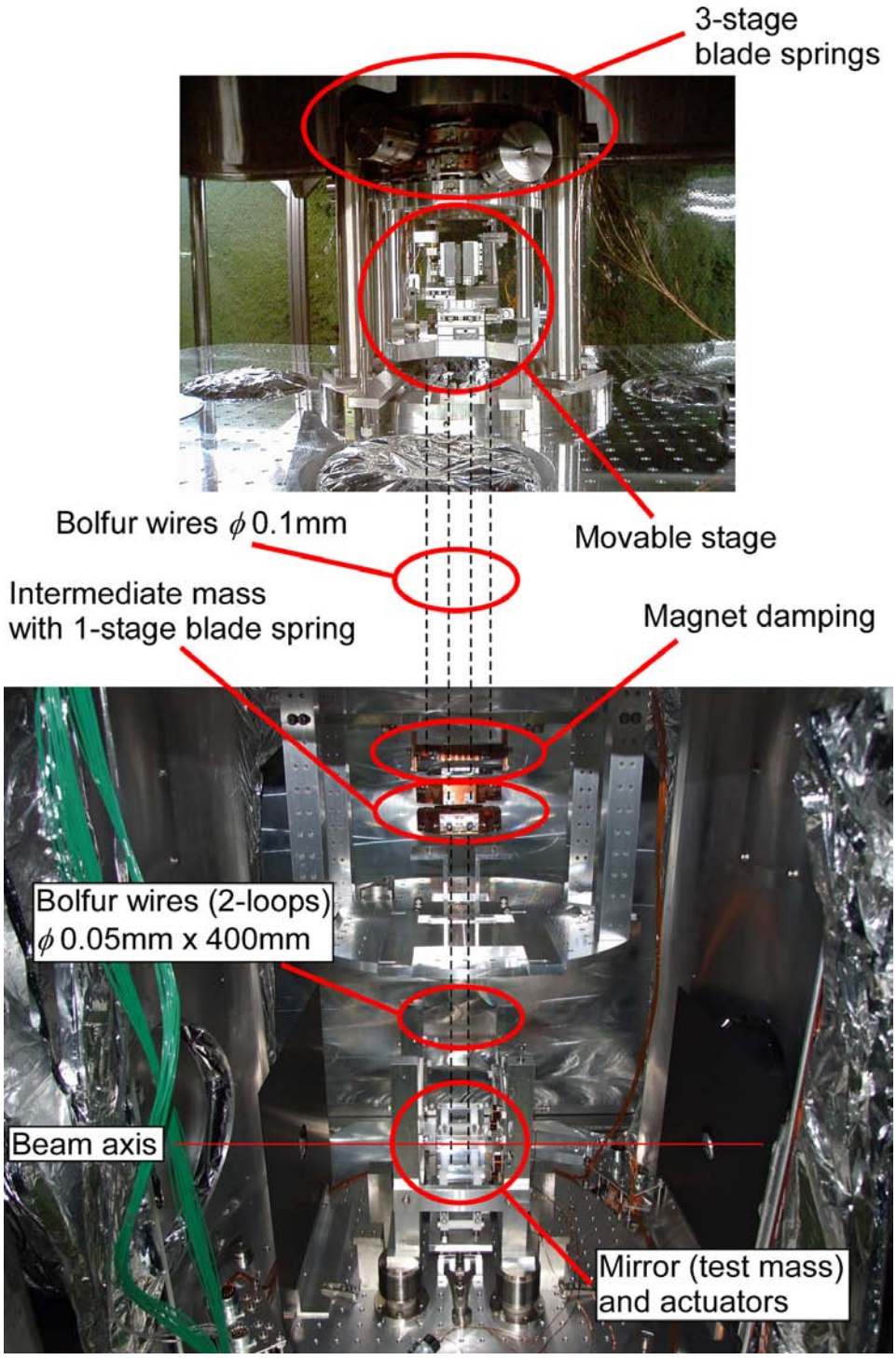

Figure 4.6: Photograph of the suspension system.

4.2.4 Multistage control system

To suppress the frequency noise, multistage control [50] is employed in CLIO. The multistage control can stabilize the laser frequency fluctuation by the small fluctuation of cavity and can maintain a wide control band. The fluctuation of the MC mirrors is stabilized by that of the main cavity. The stabilized MC fluctuation is added to the main cavity fluctuation, which is fed back to the laser frequency fluctuation (see Fig. 4.4). The frequency fluctuation, $\delta\nu$, of the laser and the mirror displacement, D_S, are related by

$$\frac{\delta\nu}{\nu} = \frac{D_S}{L}, \tag{4.10}$$

where ν is the laser frequency and L is the cavity length. The left term, involving the frequency fluctuation, is made equal to the right term, which gives the stability of the cavity, using the control. Figure 4.7 shows a block diagram of the multistage servo systems. Each block represents the transfer function of the servo circuit, C, the actuator response or the PD response, H, and the cavity response (cavity pole), P. ν is the frequency fluctuation. From Fig. 4.7, the frequency fluctuations at each location in this servo can be described as

$$\begin{aligned}\nu_1 = \nu_0 - [&\nu_2 P_{\rm MC} H_{\rm MC,PD} + N_{\rm MC} + (\nu_3 P_{\rm IN} H_{\rm IN,PD} + N_{\rm IN}) C_{\rm IN} C_{\rm FA}] \\ &\times C_0 (C_{\rm PZT} H_{\rm PZT} + C_{\rm EOM} H_{\rm EOM})\end{aligned} \tag{4.11}$$

$$\begin{aligned}\nu_2 = \nu_1 - \nu_{\rm MC} \\ + [(\nu_3 P_{\rm IN} H_{\rm IN,PD} + N_{\rm IN} C_{\rm IN} C_{\rm MC} + N_{\rm MC,END})] H_{\rm MC,END}\end{aligned} \tag{4.12}$$

$$\nu_3 = \nu_4 - \nu_{\rm IN} \tag{4.13}$$

$$\begin{aligned}\nu_4 = \nu_1 P_{\rm MC} + (1 - P_{\rm MC}) \nu_{\rm MC} \\ - (1 - P_{\rm MC}) [(\nu_3 P_{\rm IN} H_{\rm IN,PD} + N_{\rm IN} C_{\rm IN} C_{\rm MC} + N_{\rm MC,END})] H_{\rm MC,END}\}.\end{aligned} \tag{4.14}$$

These equations include the effects of all possible noises. When we assume $N_{\rm MC,END} = N_{\rm IN} = N_{\rm MC} = 0$, $C_{\rm IN} C_{\rm MC} P_{\rm IN} H_{\rm IN,PD} H_{\rm MC,END} \gg 1$, and $P_{\rm MC} = 1$, the frequency fluctuation of the incident laser, ν_4, is approximately expressed

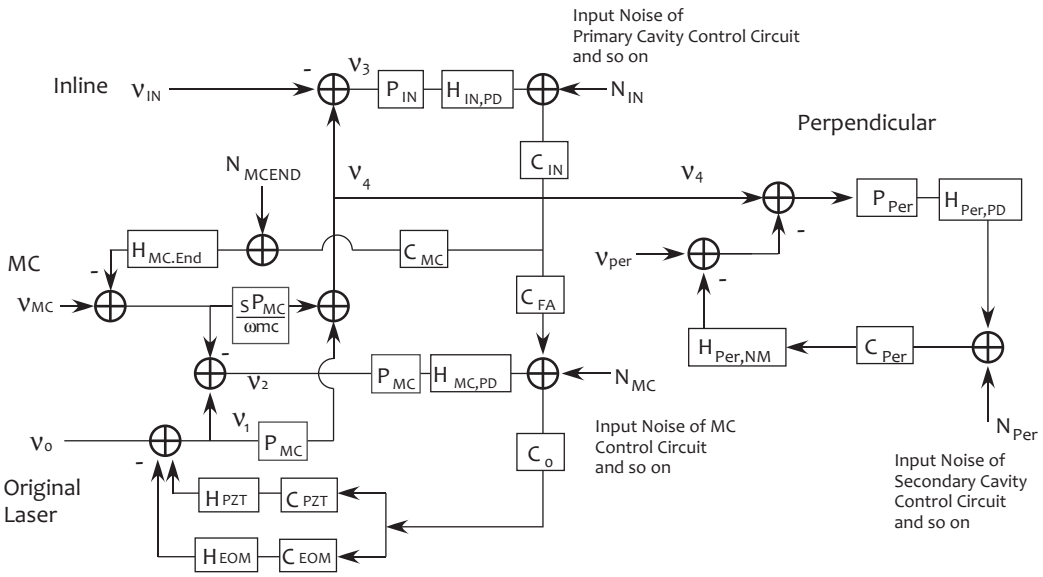

Figure 4.7: Block diagram of the servo systems (drawn with Dr. Miyoki).

as

$$\nu_4 = \frac{G_{\rm MC} G_{\rm IN}}{1 + G_{\rm MC} G_{\rm IN}} \nu_{\rm IN}, \tag{4.15}$$

where

$$G_{\rm MC} = C_0 (C_{\rm PZT} H_{\rm PZT} + C_{\rm EOM} H_{\rm EOM}) H_{\rm MC,PD} \tag{4.16}$$

$$G_{\rm IN} = C_{\rm IN} P_{\rm IN} H_{\rm IN,PD} (C_{\rm FA}/H_{\rm MC,PD} + C_{\rm MC} H_{\rm MC,END}) \tag{4.17}$$

are used. Here, G is the open-loop transfer function (not the power spectrum density despite the use of the same symbol in the previous chapter). Equation (4.15) implies that ν_4 can be suppressed to $\nu_{\rm IN}$ using a large servo gain of the MC loop, $G_{\rm MC}$, and that of the inline loop, $G_{\rm IN}$.

4.3 Calibration

4.3.1 Mass lock

From the feedback signal sent to the coil-magnet actuators, a differential displacement between the two arm cavities, which corresponds to a GW signal, can be obtained. Figure 4.8 shows a block diagram of the servo loop in the coil-magnet actuators. The transfer functions of each component are symbolized by blocks. A feedback signal, fb, is extracted through a whitening filter. According to Fig. 4.8, the displacement noise (sensitivity), Ds, is calibrated using

$$Ds = \frac{fb \times G_{\mathrm{CL}} \times A}{W}. \tag{4.18}$$

Here, $G_{\mathrm{CL}} =\mid (1+G)/G \mid$ is the closed-loop gain, G is the open-loop transfer function in the servo loop, A is the actuator response of the coil-magnet actuator, and W is the absolute value of the transfer function of the whitening filter. fb and G_{CL} in Eq. (4.18) are measured each time because they depend on the filter gain, which is tuned frequently. W and A are used after fitting.

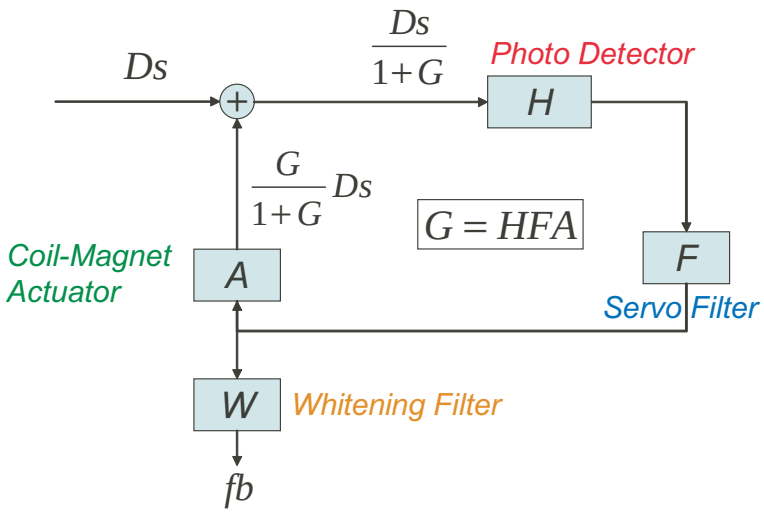

Figure 4.8: Block diagram of the mass lock servo.

4.3.2 Closed-loop gain

The open-loop transfer function, G, can be calculated from G_{CL}. Figure 4.9 shows the measured G_{CL} and the calculated G. It was found that the unity gain frequency (UGF) is 156 Hz and the phase margin is 54°. G cannot be determined precisely below 30 Hz because the magnitude of G_{CL} reaches unity; a small fluctuation of G_{CL} corresponds to a large fluctuation of G.

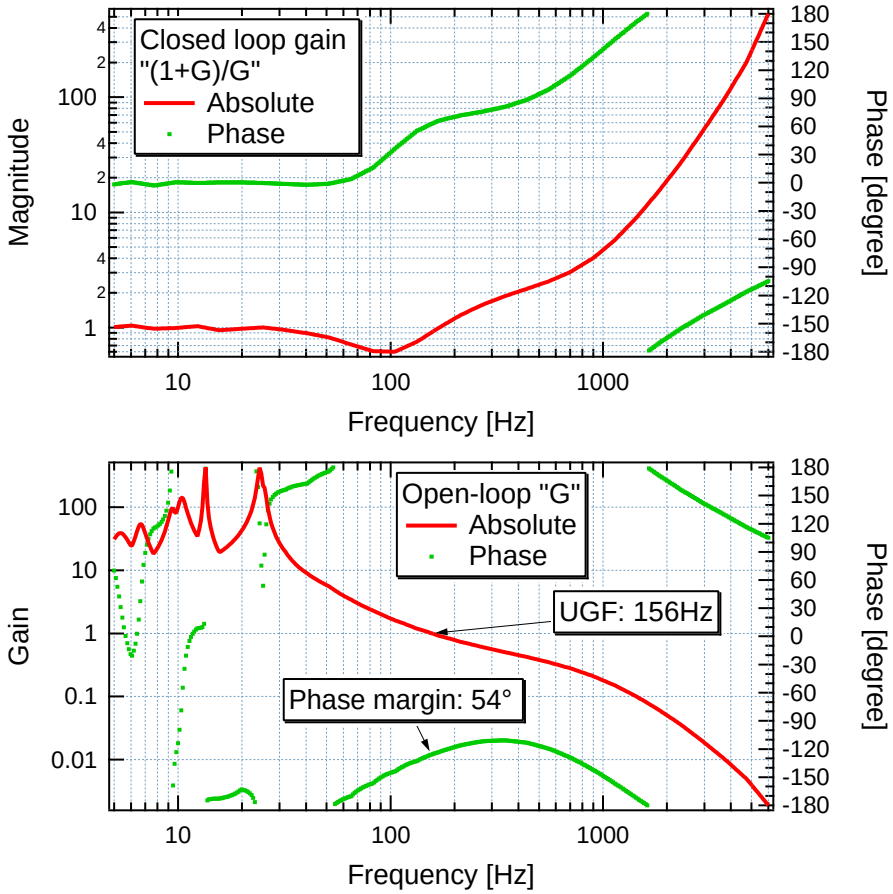

Figure 4.9: Closed-loop gain and open-loop gain.

4.3.3 Actuator response

The actuator response is the transfer function from the driver input voltage to the mirror displacement. The coil-magnet actuator response at the front mirror is measured using a Michelson interferometer constructed with front mirrors and the BS. Figure 4.10 shows a block diagram of the locking of the

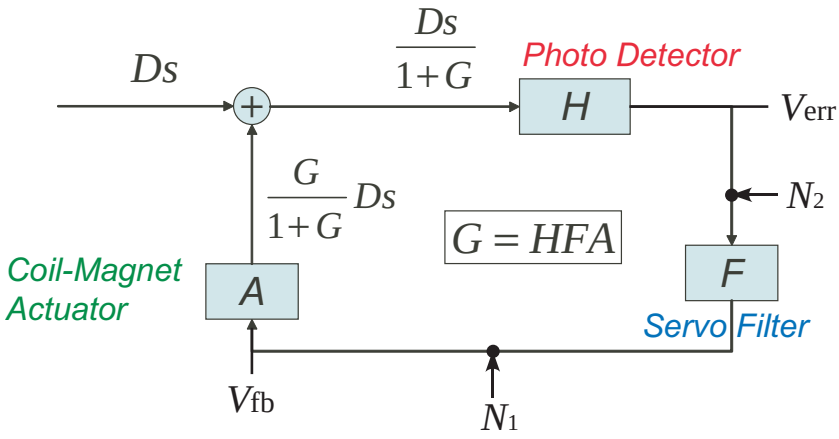

Figure 4.10: Block diagram of the locking of the Michelson interferometer.

Michelson interferometer. D_S is the natural fluctuation of the front mirrors. When a noise source N_1 is injected into this servo loop with $N_1 A \gg D_S$ at the point shown in Fig. 4.10, the feedback signal, $V_{\rm fb}$, and the error signal, $V_{\rm err}$, are expressed as

$$V_{\rm fb} = \frac{N_1}{1+G} \tag{4.19}$$

and

$$V_{\rm err} = \frac{N_1 AH}{1+G}, \tag{4.20}$$

respectively. The transfer function of these signals is, thus,

$$T_{\rm AH} = \frac{V_{\rm err}}{V_{\rm fb}} \tag{4.21}$$

$$= AH. \tag{4.22}$$

Equation (4.22) is also obtained by injecting the noise source N_2 before the servo filter. The actuator response, A, is obtained by measuring $T_{\rm AH}$ and the

PD response, H. The output signal of the PD with the Michelson interferometer is given by

$$V_{\mathrm{PD}} = \frac{1}{2} V_0 \sin\left[2\pi\Big(\frac{x}{\lambda/2}\Big)\right]. \tag{4.23}$$

Here, x is the displacement of the mirrors, λ is the wavelength of the laser, and V_0 is its amplitude, given by $V_0 = V_{\mathrm{max}} - V_{\mathrm{min}}$. In the midfringe lock ($x = \lambda/8 + \lambda n/2$), the PD response is

$$H = \left.\frac{\partial V_{\mathrm{PD}}}{\partial x}\right|_{x=\mathrm{mid}} \tag{4.24}$$

$$= \frac{1}{2} V_0 \frac{4\pi}{\lambda} \cos\Big(\frac{4\pi x}{\lambda}\Big)\Big|_{x=\mathrm{mid}} \tag{4.25}$$

$$= \frac{2\pi V_0}{\lambda}. \tag{4.26}$$

Using Eq. (4.22), the actuator response is written as

$$A = \frac{\lambda}{2\pi V_0} \times T_{\mathrm{AH}}. \tag{4.27}$$

T_{AH} is fitted using a simple second-order pole (see appendix B) for a wideband application. Figure 4.11 shows the fitting of T_{AH} and the actuator response to the background noise described in the section 5.3. In this case, only two coil-magnet actuators, which are oriented horizontally, are driven. The actuator response at 100 Hz, A_{100}, is 2.2×10^{-11}. The resistance of 100 Ω is used for the voltage-current conversion in the coil driver.

The actuator response of the end mirror is measured using the calibrated actuator of the front mirror. The setting used to measure the end actuator response is shown in Fig. 4.12. In this case, the Michelson interferometer is also locked by the servo with the front mirror. When the noise source is injected into the end actuator, the feedback signal to the front mirror is given by

$$V_{\mathrm{fb2}} = \frac{N_{\mathrm{s}} A_{\mathrm{E}} H F}{1 + G}, \tag{4.28}$$

where $G = HFA_{\mathrm{F}}$. If we assume that the parameter γ is the ratio between the responses of the front actuator and the end actuator,

$$A_{\mathrm{E}} = \gamma A_{\mathrm{F}}, \tag{4.29}$$

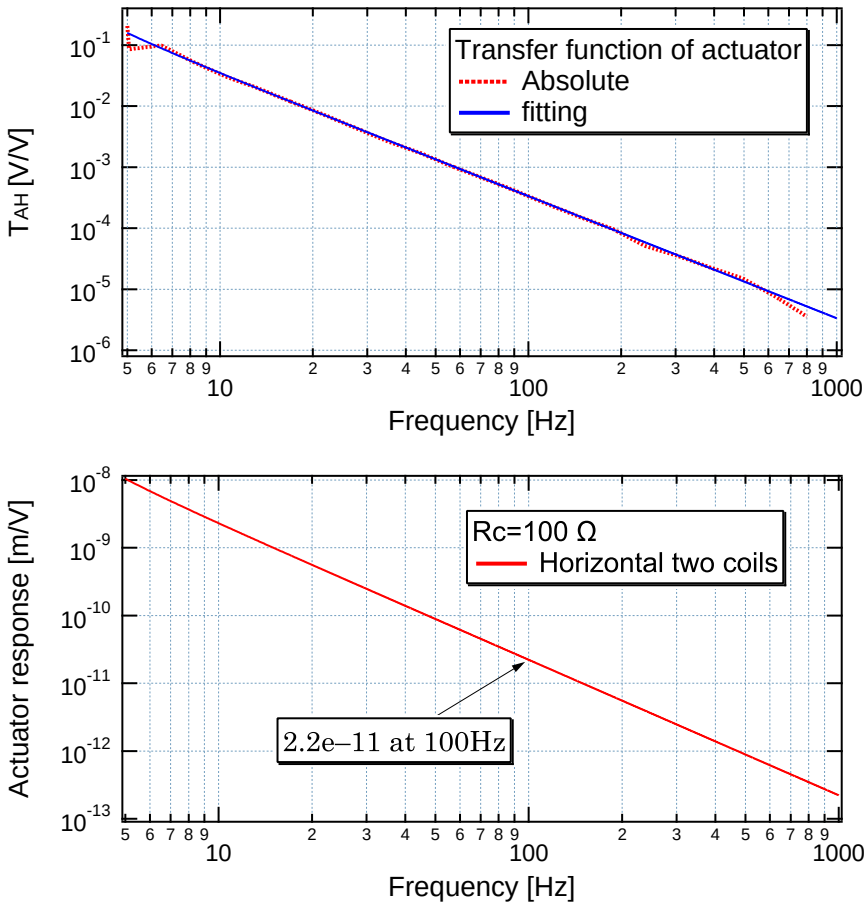

Figure 4.11: Actuator response.

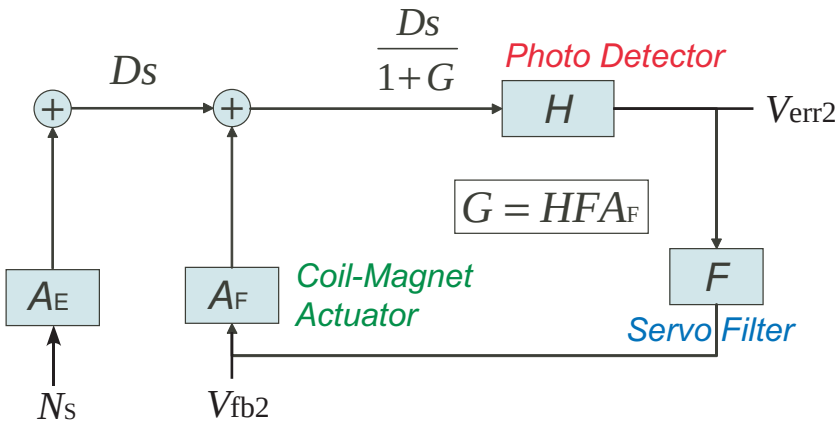

Figure 4.12: Block diagram measuring the response of the end actuator.

then γ is measured by the transfer function

$$\frac{V_{\rm fb2}}{N_{\rm s}} = \frac{A_{\rm E}HF}{1+G} \tag{4.30}$$

$$= \frac{\gamma A_{\rm F}HF}{1+G} \tag{4.31}$$

$$= \gamma\frac{G}{1+G} \tag{4.32}$$

$$\approx \gamma. \qquad (G \gg 1) \tag{4.33}$$

4.3.4 Whitening filter

The fitting function of the whitening filter consists of a combination of poles, zeros, and high-pass filters (see appendix B). The function is well fitted to the measured data as shown in Fig. 4.13. The characteristic parameters are shown in Table 4.3. The combination of the poles and zeros are determined from the circuit diagram.

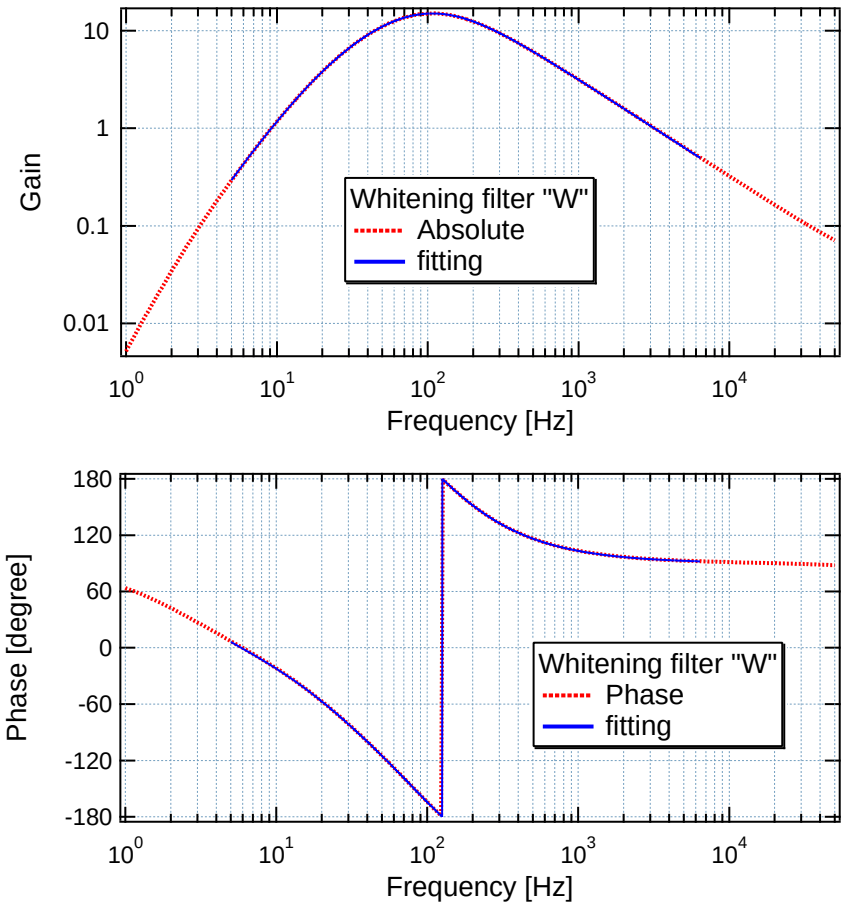

Figure 4.13: Measured transfer function of the whitening filter and its fitting.

Table 4.3: Fitting parameters of the whitening filter. The fitting function consists of three first-order high-pass filters and one first-order pole. f_h and f_p are corner frequencies of each high-pass filter and the pole, respectively.

Parameter	Value
factor	–27.5
f_h1	2.25
f_h2	22.7
f_h3	91.4
f_p1	116

4.4 Sensitivity

4.4.1 Progress of noise hunting and current best sensitivity

CLIO displacement noise has reached the predicted thermal-noise levels. Figure 4.14 shows the improvement of the displacement noise from before noise hunting to the thermal noise experiment described in section 5.3. The best floor sensitivity is $2.6 \times 10^{-19}\,\mathrm{m}/\sqrt{\mathrm{Hz}}$ at 250 Hz. In the frequency region of 20 Hz to 80 Hz, the spectrum is close to the suspension thermal noise, which originates from wire-material dissipation due to structure damping (internal damping [19]). The theoretical prediction was calculated using the Q-factor of the pendulum of 10^5, which was estimated from the measured Q-factors of violin modes. The mirror thermal noise is also close to the sensitivity and was estimated from the bulk thermal noise of the thermoelastic damping, which is in agreement with the red line in Fig. 4.1.

The noise hunting for the CLIO interferometer has progressed at room temperature. The improvement of the broad region from 20 Hz to 300 Hz is mainly due to avoiding the pendulum thermal noise due to eddy currents in the coil holder, which were induced by magnets glued onto the mirror. In

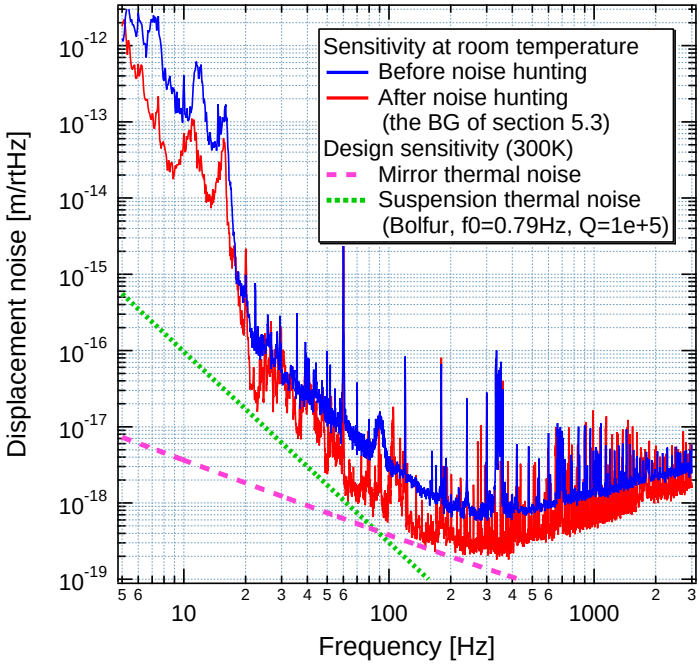

Figure 4.14: Improvement of the sensitivity in 2008; The red and blue solid lines show the measured sensitivity after noise hunting (the BG noise of section 5.3) and before noise hunting, respectively. The green dotted line shows the estimated suspension thermal noise from wire-material dissipation using the Q-factors of violin modes. The pink dashed line indicates the calculated mirror thermal noise due to thermoelastic damping of the substrate.

the high-frequency region, repairing a malfunction of the servo circuits contributed to the achievement of the shot noise. The use of thinner suspension wires made of Bolfur [41], whose diameters were changed from 0.1 mm to 0.05 mm, shifted the violin modes to higher frequencies, so as to separate the skirts of the violin modes from the region of mirror thermal noise. One reason for the improvement at approximately 10 Hz was the removal of magnets on the upper mass for extended actuation, which had been shaken by the damping magnets.

The greatest contribution toward improving the sensitivity was to identify

and remove the pendulum thermal noise due to the coil holder with a slope of f^{-2}. We emphasize that this is not suspension thermal noise. The design sensitivity was calculated to be limited by the suspension thermal noise with a slope of $f^{-5/2}$, which originates from wire-material dissipation of the internal damping [19] (Eq. (3.43)). On the other hand, the thermal noise due to the coil holder was caused by mechanical losses due to eddy currents in the conductive coil holder coupled with a pendulum, the details of which are explained in the next chapter.

Chapter 5

Identification of the pendulum thermal fluctuation

5.1 Pendulum thermal fluctuation

5.1.1 Categories of pendulum thermal noise

Interferometric GW detectors are a sophisticated apparatus including the compound mechanical systems. In order to reduce the thermal noise, it is necessary for the compound systems to distinguish the source of the thermal noise. From the viewpoint of the FDT, it equals to make the dissipation source clear. Pendulum thermal fluctuation is caused by several sources of dissipation coupled with the whole pendulum. Studies have been performed on the following types of dissipation: internal loss in materials used as suspension wires [19, 20], clamps of wires [21], residual air [19, 22, 23], coil-magnet actuators [24], and a reference mass with coils [25, 26]. Figure 5.1 shows the different categories of pendulum thermal noise (the same as Fig. 1.1). When it is obvious that thermal fluctuation is applied to the pendulum, the location of the dissipation source is used as the name of the noise. For instance, the thermal noise caused by the suspension wires and fibers, (1), is called the suspension thermal noise. The suspension wires have the dissi-

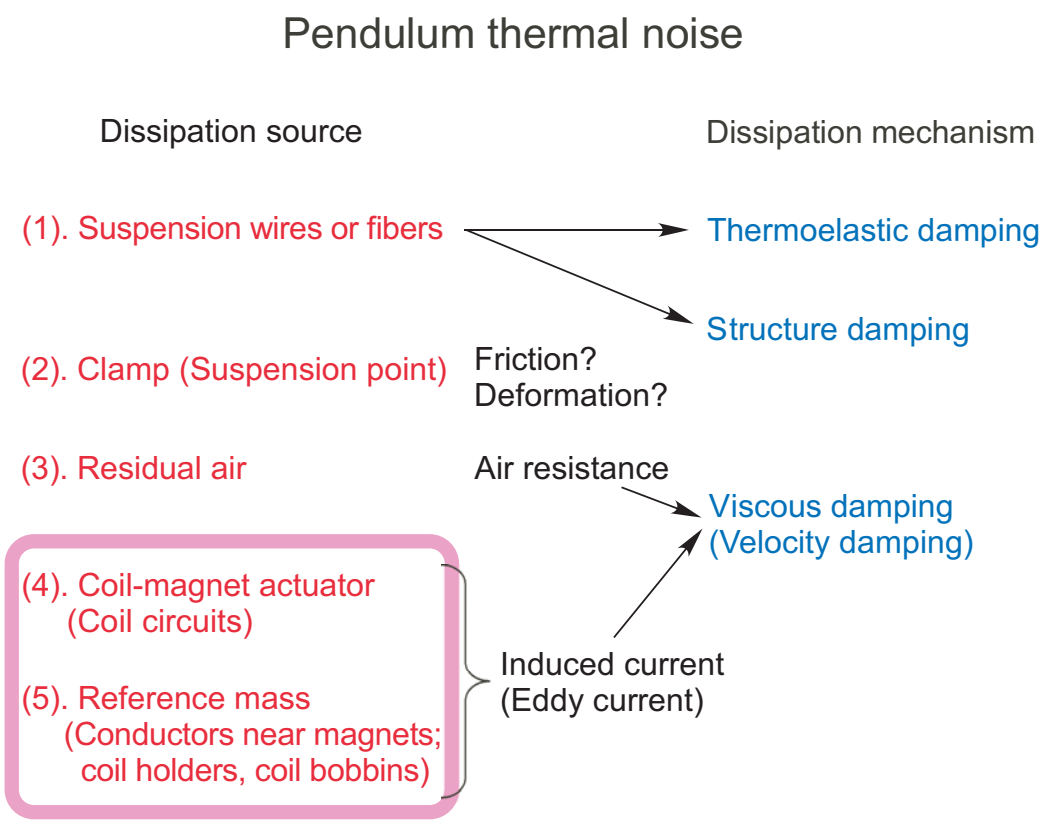

Figure 5.1: Categories of pendulum thermal noise. Sources (4) and (5) are focused on in this thesis.

pation mechanisms of structure damping and thermoelastic damping. It is possible that the wires are scraped or deformed at the clamping points. They may give rise to energy loss (2). The pendulum is subjected to air resistance by the residual air (3). Induced currents (eddy currents) are generated by magnets glued onto the mirror, which are attached to control the position of the mirror. The currents cause energy loss at resistances of conductors or circuits. The dissipations due to air resistance and induced currents are categorized as viscous damping. The dissipation mechanisms affect the frequency dependence of the pendulum thermal noise as described in Chapter 3. The methods used to reduce thermal noise, corresponding to the numbers in Fig. 5.1, are as follows.

(1) Changing the wire (or fiber) material to one with a high Q-factor

(2) The formation of delicate suspension points (clamps) or low-loss monolithic suspensions

(3) Decreasing the residual air

(4) The realization of coil drivers with a high output impedance

(5) Isolating the conductors from the magnets

Among these types of noise, attention is usually paid to only the suspension thermal noise as the fundamental noise. However, the other noises cannot be neglected. In the past, the thermal noise due to eddy currents ((4) and (5) in Fig. 5.1) was sufficiently large to compromise the design sensitivity of CLIO in the low-frequency region. This thesis centers upon the study of noise sources (4) and (5).

5.1.2 Perspective of this study

The research on thermal noise started when resonant GW detectors were built to search for GW signals [53]. The experimental investigation was continued by studying near the region of the resonance frequency of the detector [54]. For very high precision measurements whose sensitivity is limited by the thermal noise, the verification of the FDT [17, 18] not only in the resonance region but also in the off-resonance region over a wide frequency band is very important for precisely estimating the noise in the observation band and in the control band.

A rigid cavity used for laser frequency stabilization is limited by the thermal noise [55], even in an off-resonance region; also, a laser interferometric GW detector [56] is one of the most representative types of apparatus. GW detectors consist of mirrors suspended by pendulums to bring them close to a state of free mass. The thermally excited mechanical vibrations of the mirrors themselves and the suspensions impose fundamental limits on GW

detectors. Direct observations of mirror thermal fluctuation have been performed by Numata et al. [15] and Black et al. [16]. They identified the thermal fluctuation using the FDT. In these experiments it was not possible to observe the thermal fluctuation of the pendulum because the seismic noise and the mirror thermal fluctuation had large amplitudes. The seismic noise was larger than the pendulum thermal fluctuation below 100 Hz. The mirror thermal fluctuation was also larger than the pendulum thermal fluctuation above 10 Hz, because a small spot size was used on the mirrors (radii of 49 μm and 85 μm in Numata et al. [15] and 160 μm in Black et al. [16]) so as to increase the mirror thermal fluctuation. They were able to precisely identify the mirror thermal fluctuation in an off-resonance region in a wide band below the resonance frequency.

Identification of the pendulum (mechanical harmonic oscillator) thermal noise has so far been limited to a region with a width of only several times the resonance frequency [20, 22, 27]. We have achieved to identify the pendulum thermal fluctuation due to viscous damping using coil-magnet actuators ((4) in Fig. 5.1). This result is reported on Ref. [24] and this thesis (in section 5.3). This experiment is the first measurement at off-resonance in a wide band above the resonance frequency that includes the expected detection band of a GW signal around 100 Hz. This means that the measurement in this region has the following three scientific values.

- For the pendulum thermal fluctuation:

  The first identification in an off-resonance and wideband region.

- For thermal fluctuation of mechanical systems:

  The first identification above the resonance frequency in a wideband region. (Note that the measurement regions investigated by Numata et al. and Black et al. were below the resonance frequency)

- For GW detectors:

  Direct measurement in the detection band of GW signals.

To identify the thermal fluctuation of the pendulum, we made use of coil-magnet actuators, which had a number of merits. One was that the dissipation that occurred in coil circuits was easy to control and analyze. Another was that all of the parameters were measurable. Furthermore, the coil-magnet actuators did not cause any modification of the interferometer components with changes in the dissipation in the coil circuits. These merits allowed us to perform an experiment with high reliability. We were thus able to accomplish this first direct measurement using the high-sensitivity interferometer CLIO at a quiet underground site.

In the noise hunting we performed to reduce the noise in CLIO, the greatest contribution toward improving the sensitivity was to remove the pendulum thermal noise due to the coil holder ((5) in Fig. 5.1). We were able to verify the pendulum thermal noise both theoretically and experimentally. This result led to a direct verification of the noise spectrum by utilizing the estimation method by Cagnoli et al. [25] and Frasca et al. [26], and inspired a further quantitative experiment using the coil-magnet actuators discussed above.

These two results are discussed in this chapter. The verification of the pendulum thermal noise due to the coil holder is described in section 5.2, and the identification of the pendulum thermal fluctuation due to the coil-magnet actuators is described in section 5.3.

5.2 Thermal fluctuation from the coil holder

5.2.1 Theoretical estimation

The pendulum thermal noise due to the reference mass with coils (the coil holder in our case) is focused on in this section. The oscillation of the pendulum gives rise to eddy currents by electromagnetic induction in the coil holder. These currents generate Joule heat in the material of the coil holder. According to the FDT [17], the dissipation of the Joule heat causes the thermal fluctuation of the pendulum through coupling with the magnets glued onto the mirror.

The Q-factor of the pendulum, resulting from the losses of conductive materials (reference masses) near the magnets, was derived [25] as

$$Q = \frac{m\omega_0}{2\pi\sigma\left(\frac{3\mu_0\mathcal{M}}{4\pi}\right)^2 J}, \tag{5.1}$$

which was verified by not only Cagnoli et al. [25], but also Frasca et al. [26]. The detail of the derivation is described in Appendix D. Here, $\omega_0 = 2\pi f_0$, f_0 is the pendulum frequency, m is the mirror mass, σ is the median conductivity of the materials, μ_0 is the permeability, $\mathcal{M}$ is the magnetic dipole moment of the magnet, and J is a geometrical factor that depends on the shape of the conductor, given by

$$J = \int_{z1}^{z2}\int_{r1}^{r2} \frac{r^3 z^2}{(r^2+z^2)^5} dr dz. \tag{5.2}$$

Here, the conductor is assumed to be a cylinder with a centeral hole, an inner radius of $r1$, an outer radius of $r2$, and a length of $z2 - z1$ for simplicity. The center of the magnet is placed at $z = 0$, and the length from the magnet to the edge of the conductor is $z1$. The cause of thermal fluctuation is the dissipation of viscous damping, whose loss angle is $\phi = \omega/(\omega_0 Q)$, due to eddy currents in the conductor. Using the FDT (Eq. (3.37)) and applying the Q-factor given by Eq. (5.1), the thermal fluctuation of the pendulum (a harmonic oscillator) in an off-resonance region higher than the resonance

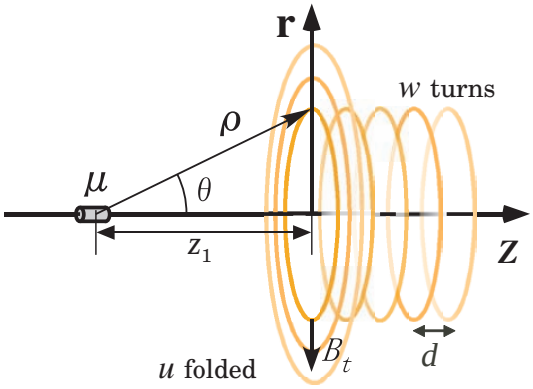

Figure 5.2: Model of a coil-magnet actuator.

frequency is approximately written as

$$G = \frac{4k_B T N}{m^2\omega^4} 2\pi\sigma \left(\frac{3\mu_0 \mathcal{M}}{4\pi}\right)^2 J. \tag{5.3}$$

k_B is the Boltzmann constant, and T is the temperature of the conductors and the pendulum. N is the number of magnet and conductor pairs, where the conductor around each magnet has a homogeneous shape.

To estimate the thermal noise due to the coil holder by Eq. (5.3) and the Q-factor of the pendulum using Eq. (5.1), the magnetic dipole moment, $\mathcal{M}$, must be determined. However, the magnetic moment is not usually easy to measure. It is practicable to utilize the coupling factor of a coil-magnet actuator to estimate the magnetic moment. Using a coil-magnet actuator, a force F given by $F = \alpha I$ can be applied to the test mass, where the coupling factor, α, is the conversion efficiency between the current, I, in a coil circuit and the force, F. This coupling factor is related to the magnetic moment of a magnet by

$$\alpha = \frac{3\,\mu_0 \mathcal{M}}{2} \sum_{s=0}^{u-1} \sum_{n=0}^{w-1} \frac{(z_1 + dn)(r_1 + ds)^2}{((z_1 + dn)^2 + (r_1 + ds)^2)^{5/2}}. \tag{5.4}$$

Here, the solenoidal coil, which consists of a conductive wire with a diameter of d, is wound around a bobbin with a radius of $r_1 - d/2$. To model the

coil we approximately consider it as a set of rings, as shown in Fig. 5.2. On the heels of the first ring, which is at a distance of $z = z_1$ from the magnet, parallel rings consisting w turns are set with a gap of d between each ring ($z = z_1 + dn$; $n = 0, 1, 2, \cdots, w - 1$). When the coil is folded into layers in the direction of increasing radius, the radius of each layer can be expressed as $r = r_1 + ds$; $s = 0, 1, 2, \cdots, u - 1$ in the case of u folds. The detail of Eq. (5.4) is explained in appendix E.

By measuring α, we can estimate the magnetic dipole moment, $\mathcal{M}$, using Eq. (5.4). The coupling factor per coil-magnet actuator, α, is yielded from Eq. (E.3),

$$\alpha = \frac{A_{100} R_{\rm c} m (2\pi \times 100)^2}{N_{\rm c}}. \tag{5.5}$$

A_{100} is the measured actuator response at 100 Hz, which is the transfer function from the driver input voltage to the mirror displacement. The response at the front mirror is measured using a Michelson interferometer constructed from the front mirrors and the BS. $R_{\rm c}$ ($R_{\rm c} = 50\ \Omega$ in CLIO) is the resistance obtained from the voltage-current conversion in the coil driver, and m is the weight of the test mass ($m = 1.9$ kg at the front mirror in CLIO). $N_{\rm c}$ ($N_{\rm c} = 4$ at the front mirror) is the number of pairs of magnets and coils.

5.2.2 Comparison between the measured and theoretical sensitivity

The sensitivity of CLIO was improved by replacing the coil holder. We attempted to prove that the noise floor using the previous coil holder originated from the thermal noise discussed in the previous section. However, the spectrum before noise hunting included some other noises. To take these noises into account, an intermediate spectrum shown in Fig. 4.14 was used as the background (BG) noise without eddy currents before noise hunting. Figure 5.3 shows a comparison between the measured spectrum before replacing the coil holder and the calculated thermal fluctuation obtained from

Eq. (5.3). The noise floor for both spectra almost matched from 20 Hz to 200 Hz. The parameters used in the estimate are indicated in Table 5.1. The spectrum for the "New coil holder" in Fig. 5.3 is employed as the BG noise because this is the first measurement using the new coil holder, which is close to the BG noise of the "Before noise hunting". For simplicity, we regarded the spectrum for the "New coil holder" from 20 Hz to 100 Hz as the "BG model," which had a slope of $f^{-5/2}$ after fitting by eye. As shown in Fig. 5.3, the sensitivity in the high-frequency region was improved because the servo circuit had already been mended. The spectrum for the "New coil-holder" was obtained after changing not only the coil holder but also other interferometer settings. Therefore, a special experiment, in which only the coil holder is replaced, is described in the next section.

The results of the theoretical evaluation did not perfectly agree with the measured spectrum in Fig. 5.3. One reason for this is a limitation of the coil-holder model. The estimated geometrical factor, J, has greater uncertainty than the other parameters, because the previous coil holder had a cubic structure around the coil, even though a cylindrical shape was assumed in the calculation from Eq. (5.2). A schematic diagram of the design and a photograph of this coil holder are shown in Fig. 5.4 and on the left of Fig. 5.6, respectively. We estimated J have a lower limit of $J = 5600$ and an upper limit of $J = 9800$. This lower limit is an underestimate because it does not include the volume of the corner of the cube not included in the cylindrical shape with $r2$ of 15 mm. A value of 9000 is obtained using the whole cube as an approximation, which corresponds to a length of $r2$ from the center of the coil to a diagonal corner (21 mm). The upper limit of $J = 9800$ is calculated by adding the effect of the outer frame (outside the cube around the coil), which is assumed to be a plate with $r1 = 21$ mm, $r2 = 32$ mm, $z1 = 10$ mm, and $z2 = 20$ mm, which is clearly an overestimate since the actual outer frame is not plate-shaped. A numerical simulation is necessary for the more precise estimation of J for a coil holder with a complex shape. Another reason for the disagreement between the measured and calculated spectra is

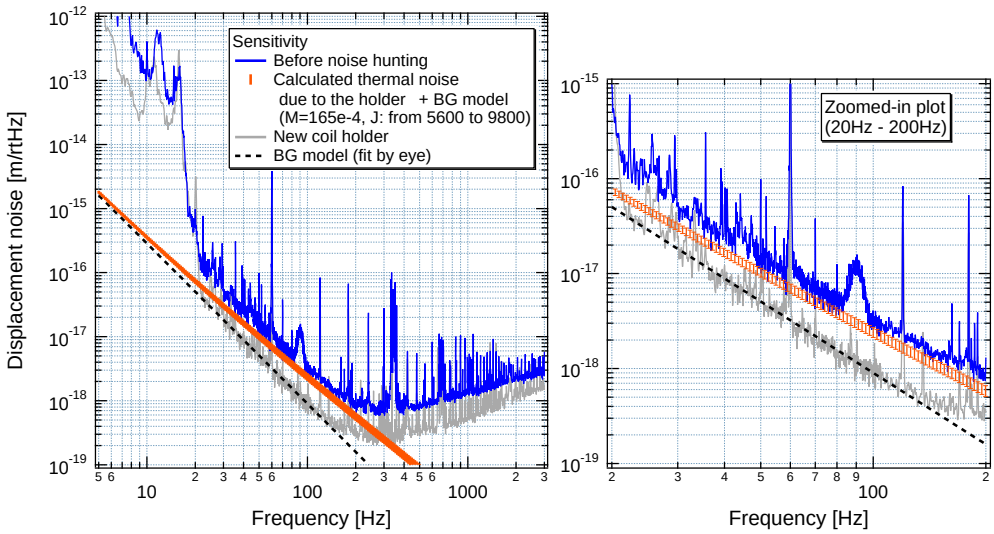

Figure 5.3: Comparison between the measured spectrum and the theoretically calculated thermal noise due to the coil holder. The blue and gray solid lines indicate the spectra measured with the previous coil-holder configuration and the new coil-holder configuration, respectively. The dashed line denotes the background (BG) model as a part of the sensitivity with the new coil holder. The orange band indicates the sum of the theoretically calculated thermal noise due to the coil holder material (J in Eq. (5.2): estimated to be from 5600 to 9800) and the BG model.

the error in the measured value of α, which is about 10%. Furthermore, it is likely that the BG noise varies in the region from 20 Hz to 50 Hz. Before noise hunting, it was possible to inject seismic noise via the coil holder fixed on an optical stage or to induce angular fluctuations of the mirrors via imperfect beam centering.

Table 5.1: Parameters used in the estimation of thermal noise. α and $\mathcal{M}$ are the average coupling factor and magnetic dipole of all magnets, respectively. The value of $r2$ for the previous coil holder indicates the length from center of the coil to a side or to a diagonal corner. The values of J were calculated from $r2$ for the two patterns (and the outer frame).

In the perpendicular front		
Parameter	Previous coil holder	New coil holder
Coil-holder (bobbin)	Al	Macor
$\sigma\,[\Omega^{-1}\mathrm{m}^{-1}]$	3.6×10^{7}	10^{-13}
$r1$ [mm]	12	—
$r2$ [mm]	15 – 21	—
$z1$ [mm]	0	—
$z2$ [mm]	20	—
Coil	Cu	Cu
N_c	4	4
w (Turns)	22	15
u (Layers)	1	2
d [mm]	0.5	0.5
r_1 [mm]	5.25	8.25
z_1 [mm]	0	5
Magnet	Nd-Fe-B	Sm-Co
Magnet size	ϕ 2 mm × 10 mm	ϕ 1 mm × 10 mm
α [N/A]	3.6×10^{-3}	4.8×10^{-4}
Estimated value		
$\mathcal{M}$ [J/T]	0.0165	0.0034
J [1/m^3]	5600 – 9000 (9800)	—
Q_holder	4.6×10^{4}	—
$\sqrt{G_\mathrm{holder}}$ at 100 Hz [m/$\sqrt{\mathrm{Hz}}$]	2.5×10^{-18}	—

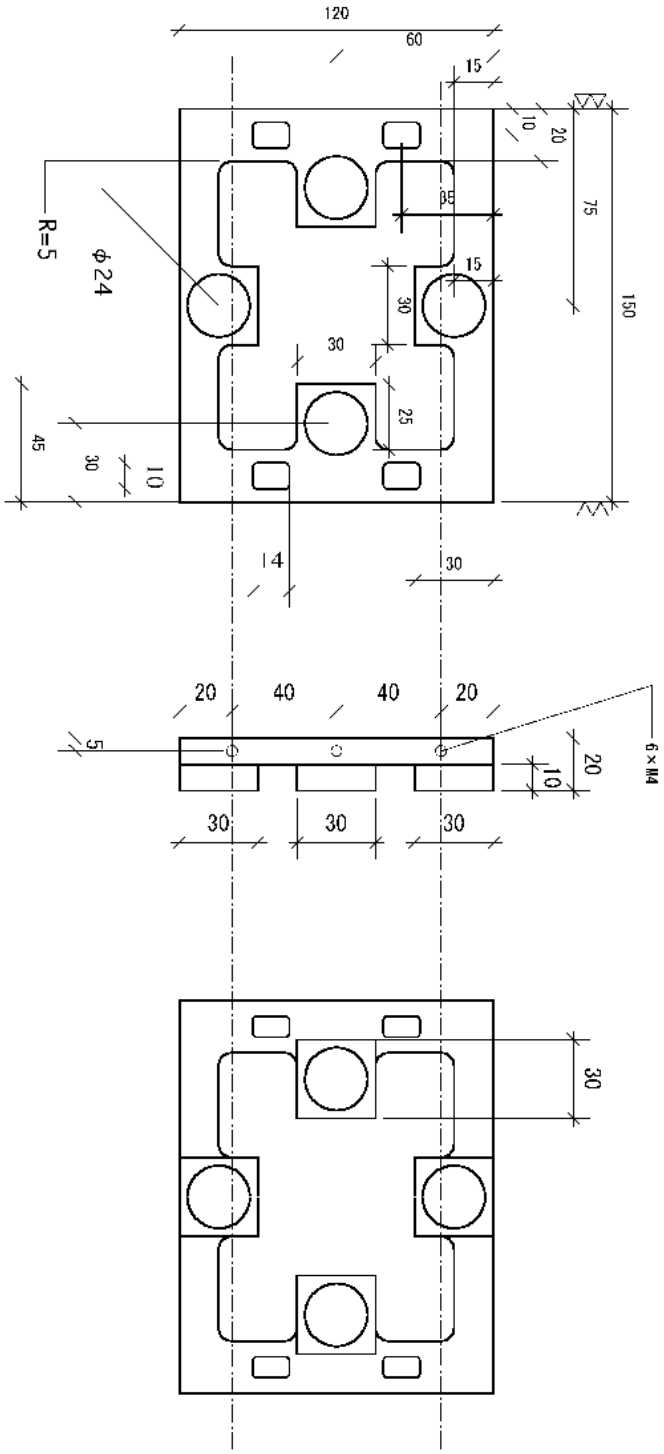

Figure 5.4: Design of the previous coil holder.

5.2.3 Experimental verification

We tested whether the sensitivity could be improved by replacing the coil holder with an electrical isolator. Figure 5.5 shows the result of this experiment. The sensitivity was improved by replacing the coil holder. Because only the coil holder was changed and the settings of the CLIO interferometer were not changed in this test, the noise floor with the previous coil holder can be regarded as being the thermal noise due to the coil holder coupled with the pendulum. In this experiment, Diflon [57] bobbins (not the "New coil-holder" in Table 5.1 and Fig. 5.3) were employed so as to suppress eddy currents. The spectrum for the Diflon bobbin was not employed as the BG noise in Fig. 5.3 because the bobbin was supported by aluminum plates with a complex shape, which did not perfectly suppress eddy currents. Aluminum was used as the material of the previous coil holder for a reason of cryogenic compatibility owing to its good thermal conduction. A precise and quantitative identification of the pendulum thermal fluctuation due to viscous damping was also performed using coil-magnet actuators [24].

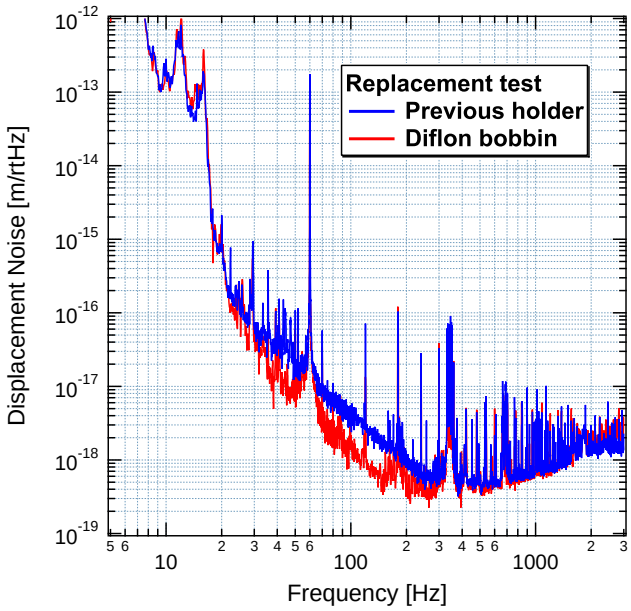

Figure 5.5: Improvement of the sensitivity obtained by replacing the coil holder. The coil holder made of aluminum was replaced with Diflon bobbins, which acted as an electrical isolator.

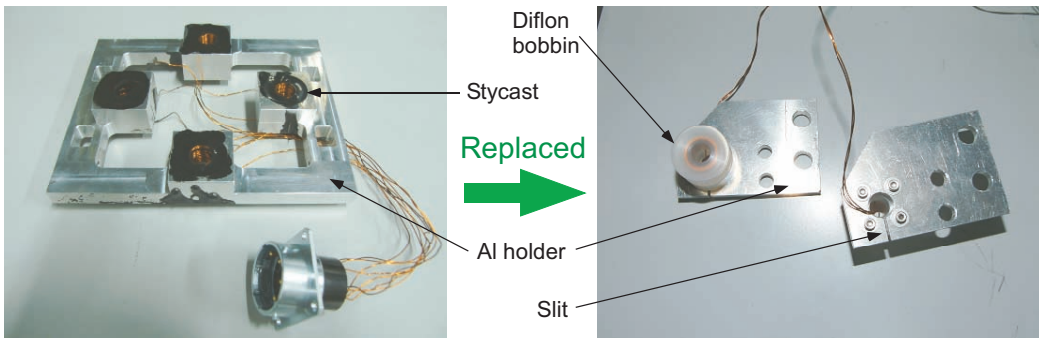

Figure 5.6: Photographs of coil holders used in the special experiment. Left: The previous coil holder. Coils are surrounded by a coil holder made of aluminum and fixed into the coil holder using Stycast [58]. Right: The Diflon bobbin. Coils are wound on Diflon bobbins fixed on an aluminum frame through thin aluminum holders with slits.

5.2.4 Improvements to the experimental setup

The coil holder was redesigned so that the pendulum could avoid mechanical losses due to eddy currents in the coil holder. The new coil holder at room temperature is shown in Fig. 5.7. The coil bobbins are made of Macor (a ceramic), which has an electrical conductivity of 10^{-13} $\Omega^{-1}\mathrm{m}^{-1}$. The aluminum frame is separated from the magnets. The diameter of the magnets was also reduced from 2 mm to 1 mm, so that their magnetic moment could be reduced, and their material was changed from Nd-Fe-B to Sm-Co as a precaution against Barkhausen noise. The current best sensitivity at room temperature, as shown in Fig. 4.14, was accomplished in this coil-holder configuration.

For cryogenic compatibility, the Macor bobbins were replaced with aluminum nitride bobbins, which is an electrical isolator with high thermal conductivity.

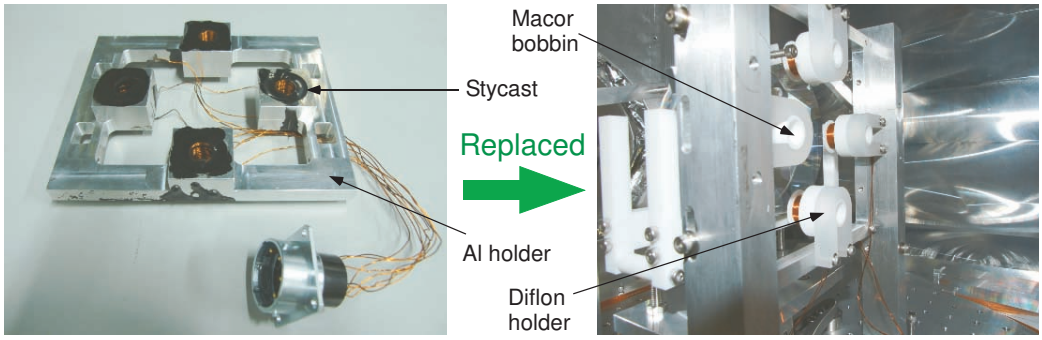

Figure 5.7: Photographs of coil holders. Left: The previous coil holder. Coils are surrounded by a coil holder made of aluminum and fixed into the coil holder using Stycast. Right: The new coil holder. Coils are wound on Macor bobbins fixed on an aluminum frame through Diflon holders.

5.3 Thermal fluctuation from the coil-magnet actuators

5.3.1 Theoretical calculation

Let us consider a pendulum and a coil circuit. Its Lagrangian is given by a quadratic form of canonical parameters, x and I, as follows;

$$\mathcal{L} = -\frac{1}{2}kx^2 + \frac{1}{2}LI^2 + \zeta xI, \tag{5.6}$$

where x is the displacement of the mass (mirror), I is the current in the coil circuit, and L is the inductance of the coil. A force, F, applied to the mass and the voltage, V, induced in the circuit are calculated using the Euler-Lagrange equations:

$$F = \frac{d}{dt}\left(\frac{\partial \mathcal{L}}{\partial \dot{x}}\right) - \frac{\partial \mathcal{L}}{\partial x} = kx - \zeta I, \tag{5.7}$$

$$V = \frac{d}{dt}\left(\frac{\partial \mathcal{L}}{\partial \dot{I}}\right) - \frac{\partial \mathcal{L}}{\partial q} = L\frac{dI}{dt} + \zeta\frac{dx}{dt}. \tag{5.8}$$

When the inertia of the pendulum mass is taken into account, a term of $m(d^2x/dt^2)$ should be added to the front of kx in Eq. (5.7). In addition, when actual coil circuits have a resistance, R, then, RI should be added to the part of $L(dI/dt)$ in Eq. (5.8). By the Fourier transformation, they are rewritten as

$$\tilde{F} = m(\omega_0^2 - \omega^2)\tilde{x} - \zeta\tilde{I}, \tag{5.9}$$

$$\tilde{V} = i\omega\zeta\tilde{x} + (i\omega L + R)\tilde{I}, \tag{5.10}$$

where $\omega_0 = 2\pi f_0$ (f_0 is the resonant frequency of the pendulum). These equations express the equations of motion of the mechanical system and the circuit, respectively. Its matrix expression is given by

$$\begin{pmatrix} \tilde{F} \\ \tilde{V} \end{pmatrix} = \begin{pmatrix} Z_{\mathrm{m}} & -\zeta \\ \zeta & Z \end{pmatrix} \begin{pmatrix} \tilde{v} \\ \tilde{I} \end{pmatrix}, \tag{5.11}$$

where $i\omega\tilde{x} = \tilde{v}$, and impedance expressions $Z_{\rm m} = m(\omega_0^2 - \omega^2)\tilde{x}/\tilde{v}$, and $Z = i\omega L + R$ are employed. In general, Z is the sum of the coil's impedance ($i\omega L$), and that of the connected coil driver. By following the reciprocity theorem, which holds in the case of a conversion from a mechanical system to its equivalent circuit. The following relations have to be satisfied:

$$F = \alpha I, \tag{5.12}$$

$$V = \alpha v, \tag{5.13}$$

where v is the velocity of the mirror, Eq. (5.11) can be converted into

$$\begin{pmatrix} \tilde{I}_1 \\ \tilde{I}_2 \end{pmatrix} = \begin{pmatrix} \frac{1}{Z} & -\frac{\zeta}{\alpha Z} \\ -\frac{\zeta}{\alpha Z} & \frac{1}{\alpha^2}\left(Z_{\rm m} + \frac{\zeta^2}{Z}\right) \end{pmatrix} \begin{pmatrix} \tilde{V}_1 \\ \tilde{V}_2 \end{pmatrix}. \tag{5.14}$$

The subscripts of 1 and 2 indicate the coil circuit and the equivalent circuit, respectively. It should be noted that the reciprocity theorem can be satisfied because the non-diagonal elements have the same notation of $-\frac{\zeta}{\alpha Z}$. This relation is also valid in the case of $\zeta = \alpha$. Equation (5.12) implies that a current inside the coil circuit causes a force to be applied to the mirror. Equation (5.13) implies that the motion of the pendulum induces an electromotive force. They are related by the same factor, α, which is a coupling factor of a coil-magnet actuator; this implies a reversible energy conversion

$$Fv = VI, \tag{5.15}$$

occurs between the pendulum mass and the coil circuit.

To model the pendulum, we assume a suspended mirror (test mass of m) and actuators constructed with N pairs of coil magnets. The reciprocity theorem can be satisfied using $F = N\alpha I$, instead of Eq. (5.12). The equations of motion of the pendulum and circuit are derived from Eq. (5.11) in a frequency domain as

$$m(-\omega^2 + \omega_0^2)\tilde{x} - N\alpha\tilde{I} = 0, \tag{5.16}$$

$$i\omega\alpha\tilde{x} + Z\tilde{I} = 0. \tag{5.17}$$

Here, the external force does not exist and $\zeta = \alpha$. By combining these equations, the overall equation of motion is

$$m(-\omega^2 + \omega_0^2)\tilde{x} + i\frac{N\alpha^2\omega}{Z}\tilde{x} = 0. \tag{5.18}$$

It is assumed that the magnitude of the impedance in the coil circuit is dominated by its resistance, R; it can then be considered that $Z = R$. From the imaginary part of Eq. (5.18), the Q-factor is defined as

$$Q = \frac{m\omega_0 R}{N\alpha^2}. \tag{5.19}$$

The fluctuation is characterized by the loss angle, $\phi = \omega/(\omega_0 Q)$, which indicates viscous damping caused by eddy currents in the coil circuits. Using the FDT (Eq. (3.37)), the fluctuation of a harmonic oscillator, i.e., a pendulum in an off-resonance region higher than the resonance frequency, is approximately expressed as

$$G = \frac{4k_B T N\alpha^2}{m^2\omega^4 R}. \tag{5.20}$$

k_B is the Boltzmann constant, and T is the temperature of the suspension and the coil circuits.

5.3.2 Strategy for measurement

To investigate the noise experimentally, it is necessary to control the magnitude of the noise. It is common practice to increase the noise to a level at which it can be measured. For example, in the measurements of mirror thermal noise (Numata et al. [15], and Black et al. [16]), the noise was enhanced by reducing the beam size, and the dissipation was controlled by changing the material of the mirror substrate. Our basic strategy is the same as that in other experiments. By using an actuator with strong coupling, the thermal noise of the pendulum is enhanced, and by changing the coil-circuit resistance, the dissipation is controlled. This means that we can control α and R in Eq. (5.20), which are expressed as

$$G = \frac{4k_B T N\alpha^2}{m^2\omega^4 R} \propto \frac{\alpha^2}{R}. \tag{5.21}$$

This way, we can investigate the thermal noise quantitatively. α and R were decided by estimating the thermal noises for arbitrary coil configurations.

Once we measure the coupling factor, we can obtain the magnitude of the magnetic dipole moment of the magnets, $\mathcal{M}$. The estimation of $\mathcal{M}$ enables us to calculate the coupling factor α for an arbitrary number of turns and folds of the coils, because $\mathcal{M}$ can be estimated from the formula

$$\alpha = \frac{3\,\mu_0 \mathcal{M}}{2} \sum_{s=0}^{u-1} \sum_{n=0}^{w-1} \frac{(z_1 + dn)(r_1 + ds)^2}{((z_1 + dn)^2 + (r_1 + ds)^2)^{5/2}}, \tag{5.22}$$

as described in section 5.2.1 and appendix E. Then, we devise a strategy for observing thermal noise. The Nd-Fe-B magnets used in this experiment had a value of $\mathcal{M}$ of $1.7 \times 10^{-2}\mathrm{Am}^2$.

On the basis of these estimations, we mapped the thermal-fluctuation dependance on the configuration of the coils. Figure 5.8 shows the thermal fluctuation of the pendulum, where the parameters are the numbers of turns and folds of the coil. The relations given by Eq. (5.20) and Eq. (5.22) are used in this calculation. $N_\mathrm{c} = 2$ was fixed by a limitation of the number of available coil bobbins. The resistance R of the coil circuit is related to the numbers of turns and folds by

$$R = \frac{4\,l}{\sigma \pi d^2}. \tag{5.23}$$

Here, σ is the conductivity of the coil material, and l and d are the length and diameter of the wire used to make the coils, respectively. The resistance of the relay circuit, which is measured in the"Short" *, is added to R. From Fig. 5.8, it was found that the pendulum thermal fluctuation can be observed over the background noise (about $1 \times 10^{-18}\,\mathrm{m}/\sqrt{\mathrm{Hz}}$) at 100 Hz. The shape of the coil bobbins entailed that the number of turns was fixed at 15. Under this condition, we choose the number of folds to be 6 owing to the ease of forming such coils and to observing the thermal fluctuation, as shown in Fig. 5.8. In this configuration the predicted thermal noise was $2.1 \times 10^{-18}\,\mathrm{m}/\sqrt{\mathrm{Hz}}$ at

*We used a relay circuit to control the dissipation by changing the resistance R. The detail is explained in the next section.

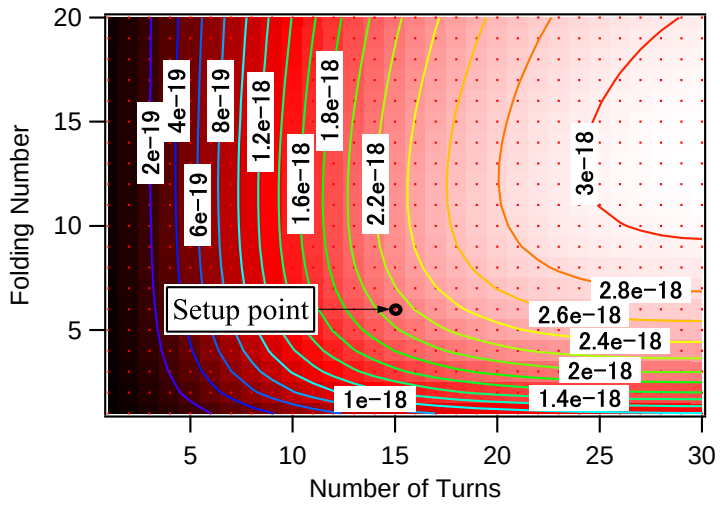

Figure 5.8: Dependence of thermal fluctuation of pendulum on the configuration of the coil at 100 Hz. The relay circuit was switched to the "Short". The "Setup point" indicates the configuration of our coils. The resistance and coupling factor depend on numbers of the turns and the folds of the coils.

100 Hz (see Fig. 5.8), and the corresponding Q-factor of the pendulum was 6.7×10^4, which is as high as that of realistic GW interferometers, and is thus not an unrealistic (extreme) value.

When two different diameters of the coil wire, d, of 0.5 mm and 0.2 mm are considered, the dependence of the thermal fluctuation on the number of folds (the number of turns is fixed at 15), is shown in Fig. 5.9. The thermal fluctuation starts to decrease when the number of folds exceeds a sufficiently large value, because the increase in R is greater than that of α^2. The peak thermal noise levels are $2.3 \times 10^{-18}\,\mathrm{m}/\sqrt{\mathrm{Hz}}$ and $2.5 \times 10^{-18}\,\mathrm{m}/\sqrt{\mathrm{Hz}}$ at 100 Hz for d of 0.5 mm and 0.2 mm, respectively. Because these values are not significantly different, the coils are made of 0.5 mm wire owing to the ease of coil formation.

Table 5.2 shows a summary of the values used and obtained in this section. It is emphasized that $\mathcal{M}$ is only used to determine the coil configuration so that the thermal noise can be estimated by measuring α using Eq. (5.20).

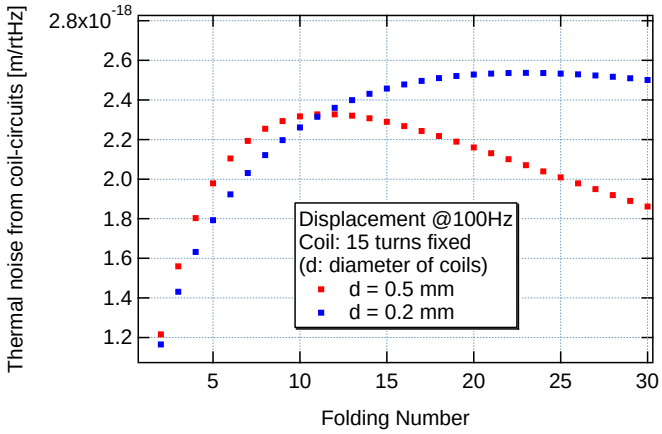

Figure 5.9: Dependence of thermal noise on the diameter of the coil wire.

Table 5.2: Determined coil configuration and estimated values: α and $\mathcal{M}$ are the average values for all magnets.

Thermal noise injection	
Parameter	Value
Coil	Cu
σ_c [Ω^{-1}m^{-1}] (300 K)	6.45×10^7
N_c	2
w (Turns)	15
u (Layers)	6
d [mm]	0.5
r_1 [mm]	8.25
z_1 [mm]	0
Magnet	Nd-Fe-B
Magnet size	ϕ 2 mm $\times$ 10 mm
α [N/A]	6.9×10^{-3}
Estimated value	
$\mathcal{M}$ [J/T]	0.017
Q_{coil}	6.7×10^4
$\sqrt{G_{100\mathrm{coil}}}$ [m/$\sqrt{\mathrm{Hz}}$]	2.1×10^{-18}

5.3.3 Experimental setup

Coil-magnet actuators are set for two mirrors in a perpendicular cavity. In order to observe the thermal fluctuation of the pendulum, we injected sufficient thermal noise into the end mirror (see Fig. 5.10), so that its fluctuation could dominate the sensitivity of CLIO, by controlling the dissipation at the coil circuits. On the other hand, the actuator of the front mirror is used to keep the cavity locked.

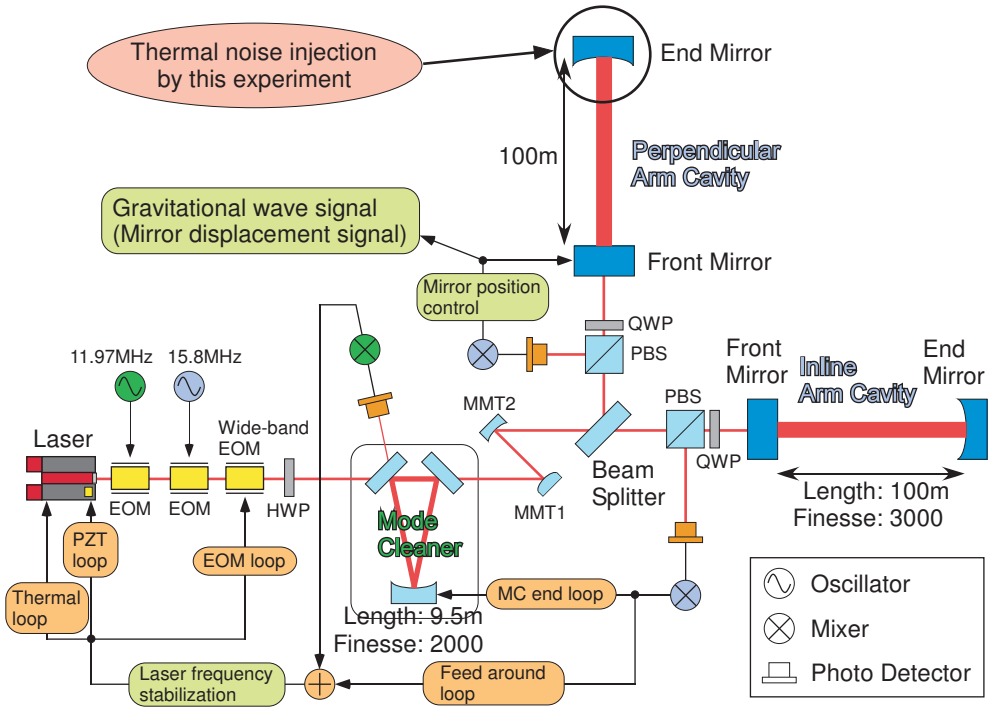

Figure 5.10: Schematic view of CLIO and its control system.

The coil-magnet actuator at the end mirror consists of two Nd-Fe-B magnets, which are glued onto the mirror, and two copper coils that approach the magnets in the horizontal direction (see Fig. 5.11 and Fig. 5.12). The Nd-Fe-B magnets have a cylindrical shape with a diameter of 2 mm and a length of 10 mm. A copper wire of 0.5 mm diameter is used for the solenoidal coils, and is wound by 15 turns times 6 layers around a ceramic bobbin, whose

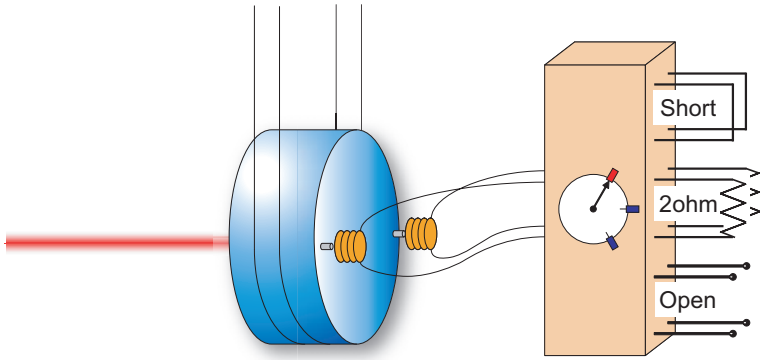

Figure 5.11: Schematic view of our experimental setup. The pendulum is composed of a sapphire mirror suspended by Bolfur [41] wires. Two coil-magnet actuators are set. The fluctuation of the pendulum is measured using the CLIO interferometer. The resistances of the coil circuits are changed by switching a relay circuit between "Short," "2ohm," and "Open." Therefore, we can control the injected thermal noise using this relay circuit.

diameter is 16.5 mm. To verify our measurement of the thermal fluctuation, the resistance R in Eq. (5.20) is changed as a parameter. R is the sum of the impedances of the coil and the connected circuit. Although a coil-driver circuit is usually used as the connected circuit, a relay circuit including resistances is used to change R in this case. The relay circuit is switched between three different resistances, which are called "Short," "2ohm," and "Open." The sum of the resistances of the coil circuits and the relay-circuit was measured to be 0.72 Ω for "Short" and 2.77 Ω for "2ohm." "Open" means that the end of the relay-circuit is open, and then R becomes infinity. From Eq. (5.20), a small R causes a large thermal fluctuation for the pendulum.

It is necessary to know the quantities in Eq. (5.20) to estimate the thermal fluctuation. In our experiment, N is 2, m is 1.8 kg, f_0 is 0.8 Hz, and T is 3.0×10^2 K. The coupling factor, α, is the actuator force applied to the mirror per unit driver output current. This is yielded from the measured actuator response, the resistance of the voltage-current conversion in the

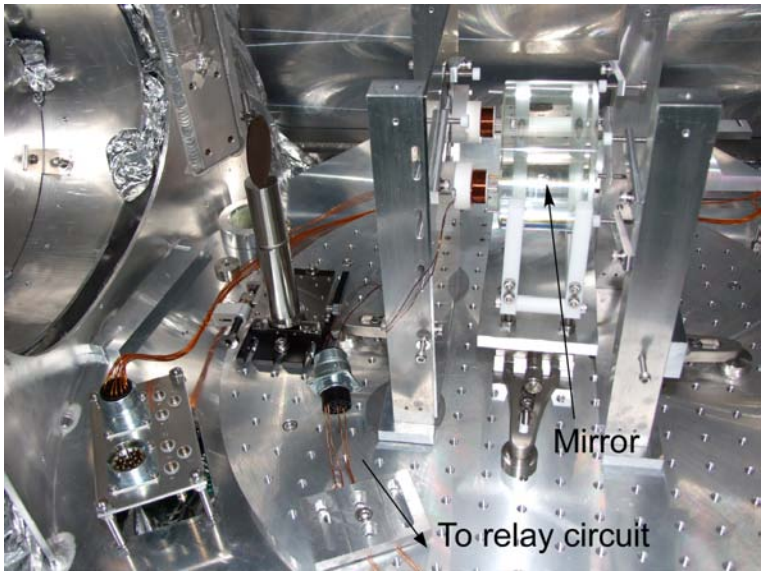

Figure 5.12: Photograph of the experimental setup.

coil driver, and the weight of the test mass. The actuator response is the transfer function from the driver input voltage to the mirror displacement. The coil-magnet actuator response at the front mirror is measured using a Michelson interferometer constructed from the front mirrors and the BS. The driver output current is obtained from the resistance of voltage-current conversion, R_c ($R_c = 50\ \Omega$ in CLIO). Using the measured actuator response at 100 Hz as A_{100} [†], the coupling factor per coil-magnet actuator is $\alpha = A_{100} R_c m (2\pi \times 100)^2 / N$. The response of the end-mirror actuator is measured by the calibrated actuator of the front mirror. Only during this calibration, the relay circuit is exchanged to a driver circuit. The value of α at the end mirror is 6.9×10^{-3} N/A.

In this experiment, other dissipations of the pendulums are adequately suppressed to below the additional dissipation of the coil circuits. The coil bobbins are made of Macor, which has an electrical conductivity of 10^{-13}

[†]The frequency of 100 Hz is at the center of our region of interest, and an accurate measurement of the transfer function is possible at this frequency.

$\Omega^{-1}\mathrm{m}^{-1}$. The pendulum is housed in a vacuum chamber, whose vacuum level is 10^{-3} Pa, so as to reduce any dissipation from residual air (see appendix C). The suspension thermal noise, which is part of the design sensitivity and originates from the dissipation of internal (structure) damping [19] of the wire material, was calculated to be below the level of the BG noise. The thermal noise from the coil-magnet actuator at the front mirror is less than the BG noise, because the output impedance of the coil driver is 10^4 Ω at 100 Hz and α is about ten times smaller than that of the end mirror.

5.3.4 Results

Figure 5.13 shows the measured spectra of the mirror displacements when we changed the resistances of the coil circuits and also shows other noises of the detector. The noise levels from 20 Hz to 400 Hz are shifted by switching the dissipation value. The measured values agree with the sums of the theoretical values estimated from Eq. (5.20) and the BG model. When the "Open" setting was chosen, a BG noise of about $1 \times 10^{-18}\,\mathrm{m}/\sqrt{\mathrm{Hz}}$ at 100 Hz was measured, since the injection thermal noise was lower than the BG level, owing to a large amount of resistance, R. For simplicity of calculations, the BG noise was modeled as $0.9 \times 10^{-18}\,\mathrm{m}/\sqrt{\mathrm{Hz}}$ at 100 Hz with a slope of f^{-2}. In the case of "Short," for instance, the noise level at 100 Hz was predicted to have a value of $2.3 \times 10^{-18}\,\mathrm{m}/\sqrt{\mathrm{Hz}}$, which includes a pendulum thermal fluctuation of $2.1 \times 10^{-18}\,\mathrm{m}/\sqrt{\mathrm{Hz}}$ and the value of the BG model. In the case "2ohm," the total value of $1.4 \times 10^{-18}\,\mathrm{m}/\sqrt{\mathrm{Hz}}$ at 100 Hz included a thermal fluctuation of $1.1 \times 10^{-18}\,\mathrm{m}/\sqrt{\mathrm{Hz}}$ and the value obtained from the BG model. We also estimated the Q-factor of the pendulum from Eq. (5.19) for these values of thermal noise. The calculated Q-factors are 6.7×10^4 for "Short" and 2.6×10^5 for "2ohm." A Q-factor of 10^5 is as large as that for pendulums in km-scale interferometers [3, 4].

For a more precise and wideband comparison between the measured spectra and theoretical calculations, Fig. 5.14 shows the difference between "Short" and "2ohm," given as $S_\mathrm{d} = (\mid S^2_\mathrm{Short} - S^2_\mathrm{2ohm} \mid)^{1/2}$; here, S_Short and

S_{2ohm} indicate the spectra of "Short" and "2ohm" in Fig. 5.13, respectively. The value of S_{d} at which the BG noise of the two noise floors is canceled, is useful for comparing the measured spectra with the theoretically calculated thermal fluctuation. The result indicates a good agreement between the measured and calculated results from 20 Hz to 400 Hz. The agreement is particularly good from 60 Hz to 300 Hz. The peak structure at approximately 50 Hz originates from the resonant motion of the coil holder at the end mirror, which is excited by the seismic motion. The noisy structure near 30 Hz originates from the BG noise.

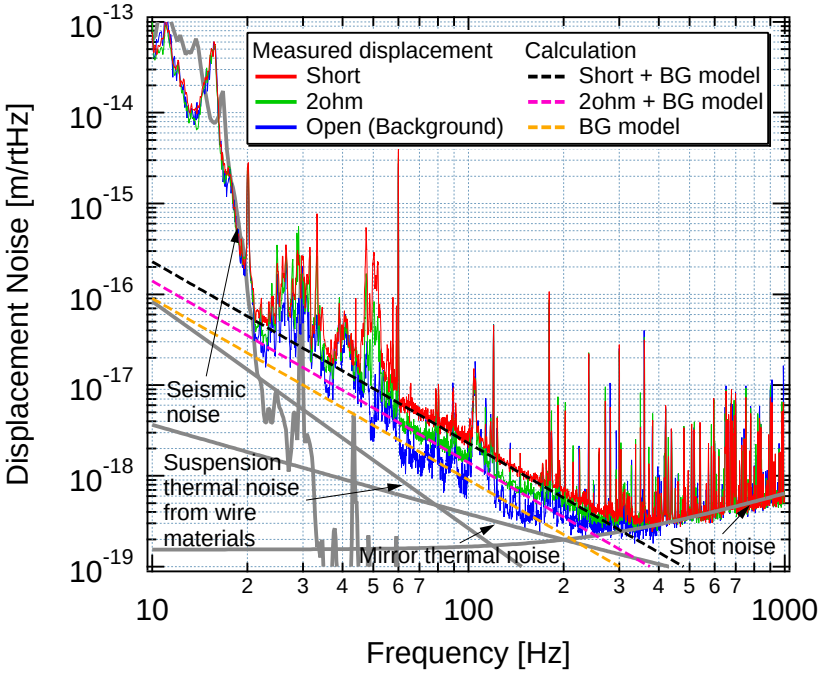

Figure 5.13: Measured spectra of the pendulum thermal fluctuation and their theoretically expected lines. The red, green, and blue solid lines denote the conditions of "Short," "2ohm," and "Open," respectively. The spectrum for "Open" corresponds to the background (BG) noise of the interferometer. The dotted lines indicate the sum of the theoretical thermal fluctuation and the value obtained from the BG model. The sensitivity is limited by shot noise above 400 Hz and by seismic noise below 20 Hz. The mirror thermal noise and suspension thermal noise (from material dissipation) were calculated to be less than the BG noise.

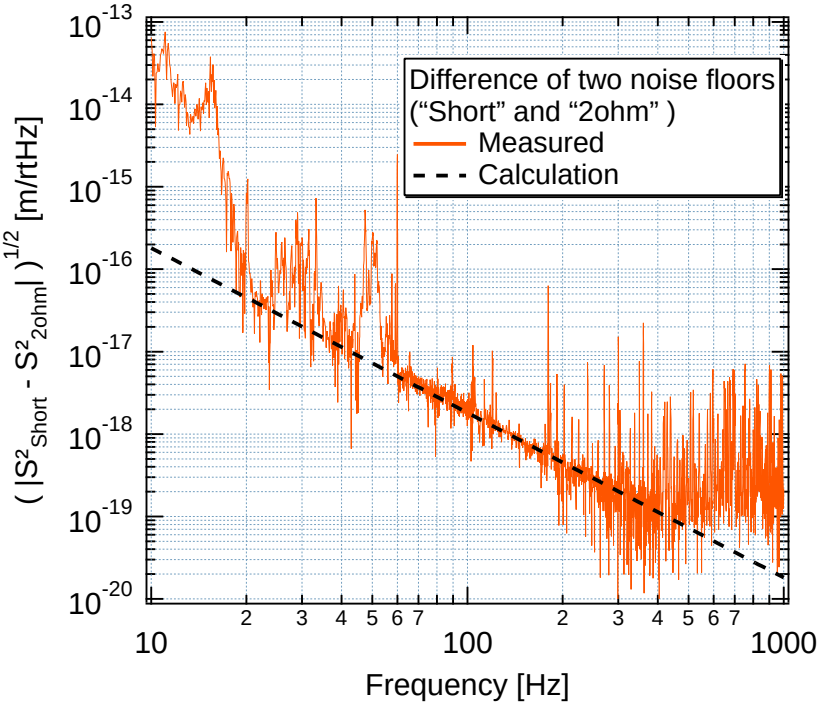

Figure 5.14: Comparison of the measured pendulum thermal fluctuation with the theoretical calculation after removing the BG noise; The orange line shows the difference between the thermal fluctuations of "Short" and "2ohm". The dashed line shows the theoretical calculation corresponding to this difference.

5.3.5 Application

The current sensitivity of CLIO is not limited by the thermal noise due to the coil-magnet actuators, but it cannot be neglected nonetheless, this thermal noise used to be sufficiently large to compromise the initial design sensitivity of CLIO in the low-frequency region. Before this research has started, the actuator response was set to be larger (coupling factor $\alpha = 3.6 \times 10^{-3}$ N/A) than that in the current configuration ($\alpha = 4.8 \times 10^{-4}$ N/A) to easily lock the CLIO interferometer. In order to suppress the servo noise after the lock state was acquired, the actuator response was reduced by adding a bypass resistance to the coil-driver circuit. The red dots denoting "Old setting" in Fig. 5.15 indicate the thermal noise due to the coil-magnet actuators with the bypass resistance. This study revealed that, with this actuator setting, the thermal noise from the coil-magnet actuators was the dominant noise source determining the CLIO sensitivity. On the basis of the analysis discussed in this section, the bypass resistance was removed and the actuator response was reduced by redesigning the actuators; this revised design is the actuator configuration of the front mirror shown in this section. The sky-blue dots denoting the redesigned actuators in Fig. 5.15 indicate the estimated thermal noise of the improved coil-magnet actuators. The difference from the frequency response for the old setting stems from the coil-driver output impedance of the redesigned actuators, which was measured to be $(1.5 \times 10^6\,\Omega) \times (1\,\mathrm{Hz}/f)$; $Z = R$ was assumed. In spite of the small magnitude of this thermal noise, the improvement of the actuator design was necessary because the sensitivity of CLIO was comparable to the world-best sensitivity of VIRGO in the low-frequency region. We are now confident that the thermal noise has been sufficiently suppressed by the quantitative estimation discussed in this thesis.

To enable long-term observation, it is necessary to control the drift of the angular alignment of the mirror. To achieve this, coil-magnet actuators with four magnets and coils are planned to be set on each of the four mirrors to control the mirror alignment. The purple dot-dash line denoting "Full

actuator setting" in Fig. 5.15 indicates the estimated thermal noise when four actuators are attached to the each of the four mirrors in the main cavity. Even if the full actuator setting is applied to CLIO, the thermal noise due to the coil-magnet actuators is lower than the design sensitivity provided each actuator has similar properties to the front-mirror actuator.

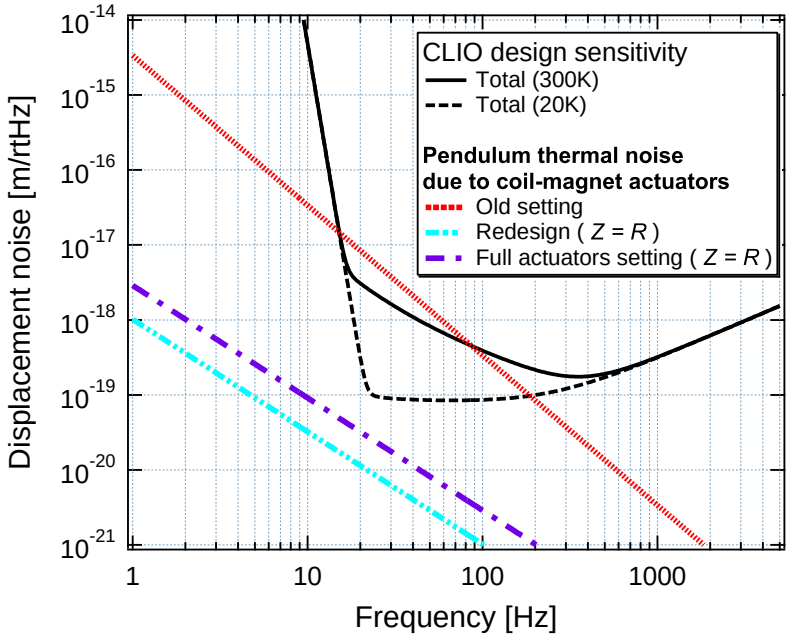

Figure 5.15: Improvement of the coil-magnet actuator design. The red dots denoting the old setting indicate the thermal noise due to the coil-magnet actuators with the bypass resistance. The sky-blue dots denoting the redesigned actuators indicate the estimated thermal noise of the improved coil-magnet actuators. The purple dot-dash line denoting "Full actuator setting" indicates the estimated thermal noise when four actuators are attached to each of the four mirrors in the main cavity.

The assumption of $Z = R$ is the worst case. Generally, the output impedance, Z, is a complex number. The thermal-noise expression including Z can be obtained from the mechanical response function. When a force, $F_{\rm th}$, is applied to the compound system of the pendulum and the coil circuits,

Eq. (5.18) is changed to

$$m(-\omega^2+\omega_0^2)\tilde{x}+i\frac{N\alpha^2\omega}{Z}\tilde{x}=\tilde{F_{\rm th}}. \tag{5.24}$$

The mechanical impedance of this system is given by

$$Z_{\rm m}(\omega)=\frac{\tilde{F_{\rm th}}}{i\omega\tilde{x}}=\frac{m(-\omega^2+\omega_0^2)}{i\omega}+i\frac{N\alpha^2}{Z}. \tag{5.25}$$

From the second FDT of Eq. (3.9), the thermal driving force is written as

$$G_f(f)=4k_BTN\alpha^2\frac{R}{\mid Z(\omega)\mid^2}. \tag{5.26}$$

The transfer function of Eq. (3.1) is given by

$$H(\omega)=\frac{\tilde{x}}{F_{\rm th}}=\frac{1}{m(-\omega^2+\omega_0^2)+i\frac{N\alpha^2\omega}{Z}}, \tag{5.27}$$

and then we obtain

$$\mid H(\omega)\mid^2=\left(\mid m(-\omega^2+\omega_0^2)+i\frac{N\alpha^2\omega}{Z}\mid^2\right)^{-1} \tag{5.28}$$

$$=\left(m^2\omega^4\left(-1+\frac{\omega_0^2}{\omega^2}\right)^2+\frac{N^2\alpha^4}{m^2\mid Z\mid^2\omega^2}\right)^{-1} \tag{5.29}$$

$$=\left(m^2\omega^4\left(-1+\frac{\omega_0^2}{\omega^2}\right)^2+\frac{\omega_0^2}{Q^2\omega^2}\frac{R^2}{\mid Z\mid^2}\right)^{-1} \tag{5.30}$$

$$=\frac{1}{m^2\omega^4}. \quad (\omega\gg\omega_0) \tag{5.31}$$

Here, the relation, Eq. (5.19) and $\mathrm{Re}[Z]=R$ are used. Using Eq. (3.11), Eq. (5.26) and Eq. (5.31), the thermal fluctuation is derived as

$$G=\frac{4k_BTN\alpha^2}{m^2\omega^4}\frac{R}{\mid Z\mid^2}. \tag{5.32}$$

This is the same as Eq. (5.20) when $\mid Z\mid$ equals to R. The thermal fluctuation takes the largest value in the case of $\mid Z\mid=R$ because of the relation $\mid Z\mid\geq R$. Note that the dissipation occurs at only the resistance R in the circuits. The coil drivers of CLIO utilize the same design as that of TAMA. The

original circuit was designed by Dr. K. Kawabe, and then improved by Dr. G. Heinzel [59]. According to the calculation for the driver circuit using a simulation tool, given in Ref. [59], the real part of the output impedance is about $(3\times10^{11}\,\Omega)\times(1\,\mathrm{Hz}/f^2)$. Figure 5.16 shows the estimate of the thermal noise from coil-magnet actuators when the real part of the output impedance in Ref. [59] is applied to Eq. (5.32). The target sensitivity of LCGT [60] is also shown in the figure. It is found that the thermal noise due to coil-magnet actuators is sufficiently below the target sensitivity. The safety factor of 10 can be kept even if the coupling factor, α, is increased by ten times. This estimate indicates that the coil-magnet actuators are an available tool for LCGT.

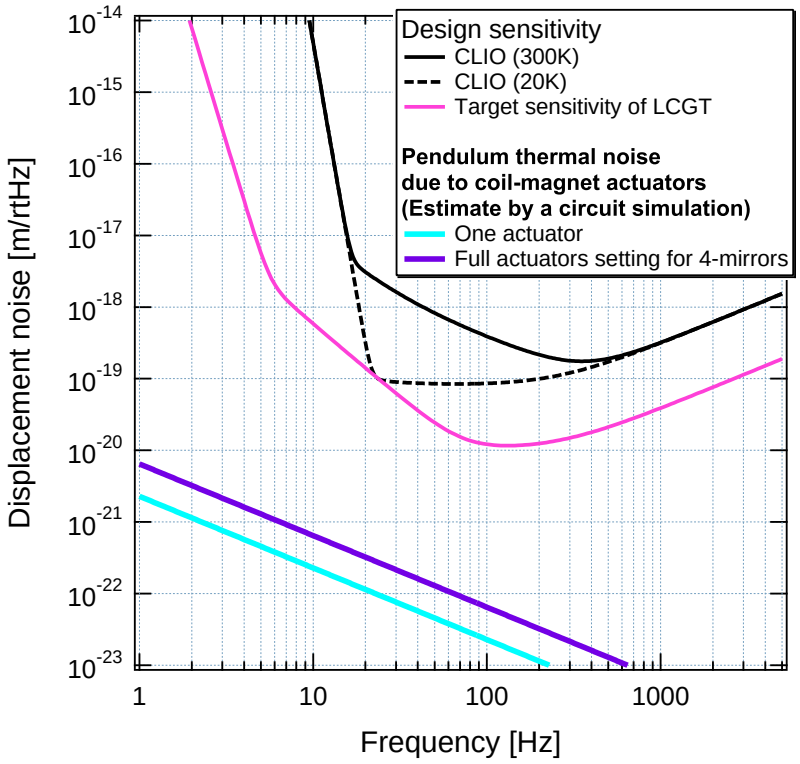

Figure 5.16: Calculated thermal-noise levels due to coil-magnet actuators and the target sensitivity of LCGT.

Chapter 6

Conclusion

6.1 Summary

6.1.1 Outline

In order to detect a gravitational wave (GW), it is necessary to design the detector sensitivity precisely and to control all kinds of noise sources in GW detectors. The thermal noise is one of the critical issues for the GW detectors. In the near future, the thermal noise is thought to limit the sensitivity. It is important to identify the thermal noise so that we can suppress it.

There are mainly two kinds of thermal noise in GW detectors, which are "the mirror thermal noise" and "the pendulum thermal noise". The mirror thermal noise was well identified by other groups by means of the direct measurements. On the other hand, identifications of the pendulum thermal noise had been limited to a region only around the resonance. This thesis focuses on the identification of the thermal fluctuation of the pendulum in a mechanical system.

The thermal noise can be estimated using the fluctuation-dissipation theorem, which indicates that an energy dissipation causes a thermal fluctuation in the thermal equilibrium. In order to reduce the thermal noise in compound mechanical systems, it is important to distinguish its dissipation source. The

pendulum thermal noise is caused by several kinds of dissipation sources. The dissipation sources of a pendulum and its mechanisms are discussed in section 5.1.1. One of the main themes of this thesis is on the pendulum thermal noise caused by eddy currents in conductors around the mirror. There are two kinds of conductive parts near the mirror: coil circuits and coil holders. The coil circuits are a part of the coil-magnet actuators for an operation of interferometers.

By the study described in this thesis, it was verified that the previous sensitivity of the Japanese GW detector CLIO (Cryogenic Laser Interferometer Observatory) was dominated by the pendulum thermal noise due to the coil holder (section 5.2). Moreover, we have achieved direct measurements of the pendulum thermal fluctuation in both off-resonant and in a wide-band region, which is close to the most expected band of GW detection (around 100 Hz). We made use of the coil-magnet actuators to control the dissipation as an injected thermal-noise source (section 5.3). The main points of sections 5.2 and 5.3 are summarized in the following section.

In general, interferometric GW detectors are a sophisticated system. In this thesis, a fundamental issue in a GW detector with regard to the thermal fluctuation was studied by a simple experiment, and we have achieved a quantitative verification of extremely small pendulum fluctuations through super-precise measurements.

6.1.2 Verification of the thermal noise due to the coil holder

Through the process to improve the sensitivity of CLIO, the sensitivity of the most important frequency region (around 100 Hz) for the GW detectors was improved (section 4.4). It was suspected that the dominant noise of the previous sensitivity around 100 Hz was due to the pendulum thermal noise coupled with coil-holder material by magnet glued onto the mirror. The identification of this noise was performed through both a theoretical and an

experimental verification.

In the theoretical verification, I calculated the pendulum thermal noise due to the coil holder material (section 5.2.1). Cagnoli et al. had estimated the quality factor from the energy loss by eddy currents (appendix D), but their estimate had not verified by the noise spectrum directly. I have shown that the noise spectrum of the CLIO sensitivity almost agreed with the theoretical estimate obtained their estimation method (section 5.2.2). Through this calculation, we employed a new method that could easily estimate the magnetic dipole moment. The magnetic dipole moment of the magnets glued onto the mirror can be estimated by measuring the actuator response owing to the modeling of a coil-magnet actuator (appendix E).

In the experimental verification, we confirmed the noise reduction by changing the coil holder from the aluminum material to electrical-isolator bobbins (diflon bobbins) (section 5.2.3). The interferometer setting was not changed except for the coil holder.

These results indicate that the noise source was the coil holder. The new coil holder with electrical isolators was designed to reduce eddy currents adequately, and then we have installed it as described in section 5.2.4.

6.1.3 Direct measurement of the pendulum thermal fluctuation

Let us consider conductors near the magnets glued onto the mirror. The coil itself remains so as to operate the interferometer even if we use a coil holder made from an electrical isolator. The analysis of the thermal noise caused by the coil-holder prompted me to measure the pendulum thermal noise from the coil-circuits directly.

I estimated this thermal noise (section 5.3.1). It was found that the value of the thermal noise could be controlled by varying parameters: the coupling factor, α, and the coil-circuit resistance, R. Then I determined a suitable coil configuration related with α to measure the thermal noise by using the

relation of Eq. (E.10) (section 5.3.2). The experiment was performed under the settings (section 5.3.3) as below.

- Thermal noise due to coil-circuits is injected to one pendulum.
- CLIO is used as a displacement sensor.
- Dissipation was changed by using three patterns of coil-circuit resistances R as "Short," "2ohm," and "Open."

The shift of the noise floor was observed and agreed with the theoretical predictions (section 5.3.4). The observed fluctuations were extremely small value of about $2 \times 10^{-18}\,\mathrm{m}/\sqrt{\mathrm{Hz}}$ at 100 Hz. By controlling these small quantity precisely, we have identified, for the first time, the thermal fluctuation of a pendulum in an off-resonant regime and in a wideband range around the GW band. This result was confirmed by a comparison between the measured thermal noise levels and a calculation based on the FDT. No other experiments had shown agreements with the FDT in this region. In other words, this is the first time to show that the FDT for the mechanical systems is valid above the resonance frequency in a wide frequency region. This is significant for fundamental physics and in the field of a superprecise measurement.

Through this study, it was found that the thermal noise from coil-magnet actuators was comparable with the design sensitivity in the old setting. We redesigned the coil-magnet actuators with low thermal noise and installed them (section 5.3.5).

6.2 Discussion

6.2.1 Verification method

Direct measurement of the thermal noise spectrum is one of the verification methods of the FDT. Especially, we convinced that we observed the thermal noise because the noise floor was shifted as the dissipation was changed. The dissipation is the most important value of the FDT. However, it was not

perfect in terms of a verification of the FDT because we changed only one parameter although the power spectrum expression of Eq. (5.20) has plural parameters. According to the FDT, the fluctuation is determined by the response from the heat bath. The fluctuation is expressed by the temperature and the mechanical conductance as Eq. (3.7). It is better for the verification of the FDT to measure the conductance or the transfer function in the same method as references of Ref. [20] and Ref. [22].

6.2.2 Coil-magnet actuator

Coil-magnet actuators are a familiar tool for actuation of mirrors. However, there are two considerable problems in terms of thermal noise as follows:

(1) The Q-factor of the mirror is degraded by attaching magnets.

(2) The Q-factor of the pendulum is degraded by induced currents on the conductors around magnets (described in this thesis).

In order to avoid these problems of (1) and (2), electrostatic actuators are studied [61], but they are not completed yet. Coil-magnet actuators have an advantage of good handling. An actuator response of electrostatic actuators is steeply changed by a distance between the mirror and the actuator plate. On the other hand, an actuator response of coil-magnet actuators has small dependence on a distance between the coil and the magnet. K. Yamamoto et al. calculated the effect of (1) and he concluded that the loss of the magnets was not a serious problem for the next-generation GW detectors [39, 62]. By taking the results of Refs. [39, 62] and this thesis into account, the complete design of the coil-magnet actuators will be capable in respect of thermal noise for the next-generation GW detectors.

6.3 Outlook

Coil-magnet actuators are useful tools for interferometer operation and for positional control in present and next-generation GW detectors. This thesis

contributes to the evaluation of this type of thermal noise in GW detectors and to the design of actuators with improved target sensitivity. The results are particularly meaningful for next-generation GW detectors because their target sensitivities will be more demanding. However, even when the mirrors and suspensions are cooled, their thermal noise is not reduced because the coil driver is at room temperature in the current settings. It means that the thermal noise generates from the coil-magnet actuators will be suppressed by cooling the coil-driver circuits in the future study.

After the experiments described in this thesis were carried out, the BG noise shown in Fig. 5.13 has been reduced and is now comparable to the suspension thermal noise due to structure damping [48]. In order to confirm whether or not the observed spectrum is due to thermal noise, a cryogenic experiment is in progress.

Appendix A

Definitions of quality factor and loss angle

The quality factor (Q-factor, or simply Q) is the smallness of damping at the resonance frequency. It is directly related to the loss angle, $\phi(\omega)$, and is defined as

$$Q = \frac{1}{\phi(\omega_0)}, \tag{A.1}$$

where ω_0 is the angular frequency at the resonance. The loss angle is equal to the energy dissipation per cycle and is defined as

$$2\pi\phi(\omega) = \frac{PT_\mathrm{c}}{E}. \tag{A.2}$$

Here, P is the energy dissipation per unit time, E is the accumulated energy in the system, and $T_\mathrm{c} = 2\pi/\omega$. Thus,

$$\phi(\omega) = \frac{P}{\omega E}. \tag{A.3}$$

Using the definition in Eq. (A.1), the Q-factor is expressed as

$$Q = \frac{\omega_0 E}{P}. \tag{A.4}$$

Appendix B

Transfer function expressed in terms of poles and zeros

A transfer function, $H(\omega)$, is given by

$$H(\omega) = \frac{\tilde{X}}{\tilde{W}} \tag{B.1}$$

in Fourier space. Here, $\tilde{W}$ is an input and $\tilde{X}$ is an output. The transfer function takes complex values, which has phase information between the input and the output. A servo loop is frequently displayed as a block diagram including the transfer function. In general, a transfer function is expressed using polynomials as follows:

$$H(\omega) = \frac{\sum_{j=0}^{M} a_j (i\omega)^j}{\sum_{k=0}^{N} b_k (i\omega)^k}. \tag{B.2}$$

Each polynomial can be expanded using a Laplace transformation ($s = i\omega$) to give

$$H(s) = \frac{a_M s^M + a_{M-1} s^{M-1} + \cdots + a_1 s + a_0}{s^N + b_{N-1} s^{N-1} + \cdots + b_1 s + b_0}, \tag{B.3}$$

where we choose $b_N = 1$. The factorization of Eq. (B.3) gives

$$H(s) = \frac{a_M (s - z_1)(s - z_2) \cdots (s - z_M)}{(s - p_1)(s - p_2) \cdots (s - p_N)}. \tag{B.4}$$

A solution of $H(s) = 0$ obtained from $(s - z_1) \cdots (s - z_M)$ is called a "zero." A solution obtained from $(s - p_1) \cdots (s - p_N)$ is called a "pole." Therefore, a transfer function can be expressed as a combination of poles and zeros. The pole and zero of the first order are given by

$$P^1(f) = \left(1 + i\frac{f}{f_p}\right)^{-1}. \tag{B.5}$$

$$Z^1(f) = 1 + i\frac{f}{f_z}. \tag{B.6}$$

These are shown in Fourier space. f_p and f_z are the corner frequencies where the frequency response is changed. These parameters uniquely determine the characteristics of the transfer function. The pole and zero of the second order are given by

$$P^2(f) = \left(1 + i\frac{f}{f_p q_p} - \left(\frac{f}{f_p}\right)^2\right)^{-1}. \tag{B.7}$$

$$Z^2(f) = 1 + i\frac{f}{f_z q_z} - \left(\frac{f}{f_z}\right)^2. \tag{B.8}$$

In these equations, there are resonant peaks giving the Q-factor, q_p or q_z, at the frequency, f_p or f_z, respectively. The expressions for the poles and zeros are used for modeling servo systems with electrical circuits. In addition, a high-pass filter of the first order can be expressed as

$$H_{\mathrm{p}}(f) = \frac{i\frac{f}{f_h}}{1 + i\frac{f}{f_h}}. \tag{B.9}$$

Here, f_h is the corner frequency.

Appendix C

Q-factor of a pendulum due to residual gas

Air resistance is the most well-known external loss of a pendulum. In GW detectors, pendulums are housed in vacuum tanks. Thus, the dilute gas is a source of dissipation called residual gas damping, which is a type of viscous damping (see Fig. 5.1). Under this dissipation, the Q-factor of an oscillator is given by [19]

$$Q_{\rm gas} = C_{\rm g} h_{\rm g} \frac{\rho \omega_0}{n_{\rm g} \sqrt{m_{\rm mol} k_B T}}. \tag{C.1}$$

Here, $C_{\rm g}$ is a dimensionless parameter that depends on the shape of the oscillator. $C_{\rm g}$ is mostly on the order of unity. The parameters $h_{\rm g}$, ρ, and ω_0 are respectively the size, density, and angular resonance frequency of the oscillator. $n_{\rm g}$ is the numerical density of the gas and $m_{\rm mol}$ is mass of the gas per molecule. In the case of a mixture of several different gases such as air, the effective mass is employed. T is the temperature of the oscillator and the residual gas. Equation (C.1) can be changed to the more useful expression of

$$Q_{\rm gas} = \frac{C_{\rm g} h_{\rm g} \rho \omega_0}{P} \sqrt{\frac{k_B T}{m_{\rm mol}}}, \tag{C.2}$$

where, the relation

$$n_{\rm g} = \frac{P}{k_B T} \tag{C.3}$$

is used from the equation of state of an ideal gas and P is the pressure of the residual gas.

In CLIO, the vacuum level is 10^{-3} Pa at room temperature. From Eq. (C.2), the Q-factor of the pendulum becomes

$$Q_{\rm gas} = 6.6 \times 10^8 \left(\frac{10^{-3}{\rm Pa}}{P}\right)\left(\frac{h}{0.1{\rm m}}\right)\left(\frac{\rho}{4\times 10^4{\rm kg/m^3}}\right)\left(\frac{f_0}{0.79{\rm Hz}}\right). \quad \text{(C.4)}$$

The pendulum Q-factor due to the residual gas (6.6×10^8) is sufficiently larger than that due to the coil holder or the coil-magnet actuators (about 10^5) in Chapter 5. Hence, this noise is suppressed to below the BG noise measured in section 5.3.

Appendix D

Q-factor of a pendulum due to a conductor surrounding a magnet

The motion of a pendulum causes eddy currents in a conductor around a magnet glued onto the mass (the mirror) of the pendulum. The dissipation of these eddy currents decreases the Q-factor of the pendulum and increases its thermal fluctuation. This model and the calculation were derived by Cagnoli et al. [25] and the detail is described in this section.

In the model, the magnet, which is regarded as a spotlike magnetic dipole moment, $\boldsymbol{\mu}$, provides a magnetic field, $\boldsymbol{B}$, at a point $\boldsymbol{\rho}$, given by

$$\boldsymbol{B}(\boldsymbol{\rho}) = \frac{\mu_0}{4\pi\rho^3}\Big\{\frac{3(\boldsymbol{\mu}\cdot\boldsymbol{\rho})\boldsymbol{\rho}}{\rho^2} - \boldsymbol{\mu}\Big\}. \tag{D.1}$$

Here, $\boldsymbol{\mu} = ja\boldsymbol{n} \equiv \mathcal{M}\boldsymbol{n}$ (the parameters j, a and $\boldsymbol{n}$ are the circular current, the enclosed area of the circle and the unit vector of $\boldsymbol{\mu}$, respectively). μ_0 is the permeability in a vacuum. When the angle between $\boldsymbol{\mu}$ and $\boldsymbol{\rho}$ is defined

as θ, the magnetic field at $\boldsymbol{\rho}$ in the direction of $\boldsymbol{\mu}$ is

$$B_n = \boldsymbol{B} \cdot \boldsymbol{n} \tag{D.2}$$
$$= \frac{\mu_0 \mathcal{M}}{4\pi\rho^3} \left(3\cos^2\theta - 1\right) \tag{D.3}$$
$$= \frac{\mu_0 \mathcal{M}}{4\pi} \frac{2z^2 - r^2}{(r^2+z^2)^{5/2}}, \tag{D.4}$$

where the magnetic moment, $\boldsymbol{\mu}$, is located at the origin and oriented to the axial direction of the z axis. $\boldsymbol{\rho}$ is oriented from the origin to a circle with a radius r whose center is at a point on the z axis (i.e., $\rho^2 = r^2 + z^2$). This coordinate is shown in Fig. E.1. Using Eq. (D.4), the magnetic flux in the circle with radius r in the $\boldsymbol{\mu}$ direction is expressed as

$$\phi = \int_S \boldsymbol{B} \cdot \boldsymbol{n}\, dS \tag{D.5}$$
$$= \int_0^r B_n \cdot 2\pi r\, dr \tag{D.6}$$
$$= \frac{\mu_0 \mathcal{M}}{2} \frac{r^2}{(r^2+z^2)^{3/2}}. \tag{D.7}$$

The motion of the mirror, given by $z = A\sin(\omega t)$, causes an electromotive force, E', to be generated at a point on the circle with radius r. E' is written as

$$E' = \frac{1}{2\pi r} \int \boldsymbol{E}\, d\boldsymbol{l} \tag{D.8}$$
$$= -\frac{1}{2\pi r} \left(\frac{d\phi}{dt}\right) \tag{D.9}$$
$$= \frac{3\mu_0 \mathcal{M}}{4\pi} \frac{zr}{(r^2+z^2)^{5/2}} A\omega\cos(\omega t). \tag{D.10}$$

From Ohm's law, $\boldsymbol{E} = \sigma \boldsymbol{J}$ (σ is the electrical conductivity), and the electric power per cycle ($2\pi/\omega$) consumed by the eddy current on the circle is

expressed as

$$dP = \frac{\omega}{2\pi} \int_{1cycle} E' J' \, 2\pi r \, dr dz \, dt \tag{D.11}$$

$$= 2\pi\sigma \left(\frac{3\mu_0 \mathcal{M}}{4\pi} \right)^2 \frac{r^3 z^2}{(r^2 + z^2)^5} A^2 \omega^2 \frac{\omega}{2\pi} dr dz \int_0^{2\pi/\omega} \cos^2(\omega t) dt \tag{D.12}$$

$$= 2\pi\sigma \left(\frac{3\mu_0 \mathcal{M}}{4\pi} \right)^2 \frac{r^3 z^2}{(r^2 + z^2)^5} \frac{A^2 \omega^2}{2} dr dz. \tag{D.13}$$

When we regard the conductor as a center-holed coaxial cylinder, the dissipation, P, produced by the whole conductor is given by

$$P = \int_{z1}^{z2} \int_{r1}^{r2} dP = 2\pi\sigma \left(\frac{3\mu_0 \mathcal{M}}{4\pi} \right)^2 \frac{A^2 \omega^2}{2}. \tag{D.14}$$

Here,

$$J = \int_{z1}^{z2} \int_{r1}^{r2} \frac{r^3 z^2}{(r^2 + z^2)^5} dr dz \tag{D.15}$$

is called the geometrical factor, which depends on the shape of the conductor.

From Eq. (A.4), the Q-factor of a system with accumulated energy E and a dissipation of P per unit time is expressed as

$$Q = \frac{\omega_0 E}{P}. \tag{D.16}$$

This is applicable to the pendulum. The accumulated energy in the pendulum is

$$E = \frac{1}{2} m \left(\frac{dz}{dt} \right)^2 + \frac{1}{2} m \omega^2 z^2 \tag{D.17}$$

$$= \frac{1}{2} m A^2 \omega^2. \tag{D.18}$$

From Eq. (D.16), Eq. (D.18), and Eq. (D.14), the Q-factor of the pendulum is given by

$$Q = \frac{m\omega_0}{2\pi\sigma \left(\frac{3\mu_0 \mathcal{M}}{4\pi} \right)^2}. \tag{D.19}$$

Note that this is the Q-factor per magnet and conductor pair. If there are N pairs, then Eq. (D.19) must be divided by N.

Appendix E

Coupling factor α and magnetic dipole moment $\mathcal{M}$

To estimate the thermal noise of a pendulum from Eq. (5.3) and Eq. (5.20), or its Q-factor from Eq. (5.1) and Eq. (5.19), it is essential to know the coupling factor of the coil-magnet actuators and the magnetic dipole moment of magnets. The coupling factor can be measured using the coil-magnet actuator efficiency. Then, the magnetic dipole moment can be estimated by modeling a coil-magnet actuator using the coupling factor.

For one coil-magnet actuator, the force

$$F = \alpha I \tag{E.1}$$

can be applied to the test mass. The coupling factor, α, is the conversion efficiency between the current, I, in a coil circuit and the force, F. The value of α per coil-magnet actuator is yielded from

$$\alpha = \frac{A_{100} R_c}{H_{100} N_{\mathrm{c}}} \tag{E.2}$$

$$= \frac{A_{100} R_{\mathrm{c}} m (2\pi \times 100)^2}{N_{\mathrm{c}}}, \tag{E.3}$$

where the suspended mirror at 100 Hz is regarded as almost a free-fall mass. Then the transfer function from the force to the displacement of the mirror H can be approximately expressed as $1/m\omega^2$. A_{100} is the measured actuator

efficiency at 100 Hz [*], which is the transfer function from the driver input voltage to the mirror displacement. The coil-magnet actuator efficiency at the front mirror is measured using a Michelson interferometer constructed from the front mirrors and the BS. $R_{\rm c}$ is the resistance of the voltage-current conversion in the coil driver, and m is the weight of a test mass. $N_{\rm c}$ is the number of magnet and coil pairs. Moreover, α is also given by

$$\alpha = \frac{A_{\rm dc}\, R_{\rm c}\, k_{\rm p}}{N_{\rm c}}. \tag{E.4}$$

Here, $A_{\rm dc}$ is the actuator efficiency at a DC voltage. $k_{\rm p}$ is the spring constant of the pendulum, given by $k = m\omega_{\rm p}^2$, where $\omega_{\rm p} = 2\pi f_{\rm p}$. $f_{\rm p}$ is the resonance frequency of the pendulum in the primary mode. Note that Eq. (E.3) is more useful than Eq. (E.4) because of its easy measurement.

The magnetic dipole moment, $\mathcal{M}$, must be known to estimate the thermal noise due to the coil holder using Eq. (5.3) and the Q-factor of the pendulum using Eq. (5.1). However, the magnetic moment is not usually easy to measure [†]. It is practicable to utilize the coupling factor of a coil-magnet actuator to estimate the magnetic moment. To model the coil-magnet actuator, we consider a magnet as a pointlike magnetic dipole moment and consider a coil as a set of rings separated by a gap of d, as shown in Fig. E.1. Note that the magnetic dipole moment is regarded as the "effective" moment because the effects of high-order terms of the magnetic moment that originate from the finite volume of the magnet or the smallness of the coil are included in the pointlike magnetic dipole moment. When we define the same magnetic dipole moment as that given by Eq. (D.1), the magnetic moment generates

[*] 100 Hz is approximately in the middle of our region of interest, and an accurate measurement of the transfer function is possible at this frequency.

[†] If the residual magnetic flux of the magnet, $B_{\rm r}$, and its volume, V, can be obtained, then the dipole moment is expressed as

$$\mathcal{M} = \frac{B_{\rm r} V}{\mu_0}. \tag{E.5}$$

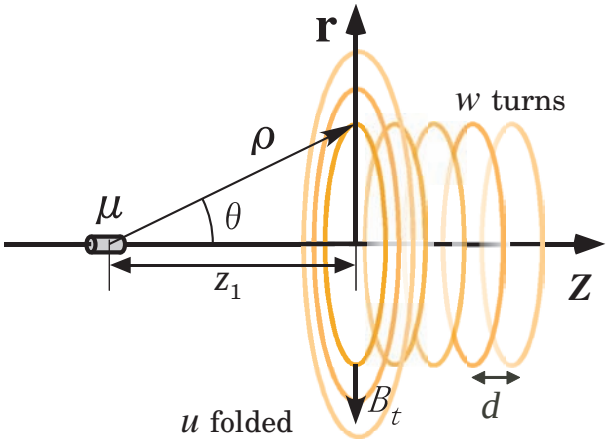

Figure E.1: Model of a coil-magnet actuator.

a magnetic field $\boldsymbol{B}$ at a point $\boldsymbol{\rho}$, which is written as

$$B_t = \frac{\mu_0 \mathcal{M}}{4\pi\rho^3}(3\cos\theta\sin\theta) \tag{E.6}$$

$$= \frac{\mu_0 \mathcal{M}}{4\pi}\frac{3zr}{(r^2+z^2)^{5/2}}. \tag{E.7}$$

Here, B_t is the magnitude of a normal vector of its magnetic field. μ_0 is the magnetic permeability. $\mathcal{M}$ is the magnitude of the magnetic dipole moment. θ is the angle between $\boldsymbol{\mu}$ and $\boldsymbol{\rho}$. The magnet lies on an axis through the center of the coil (Z axis). This magnetic field gives rise to a force of

$$F = 2\pi r I\, B_t \tag{E.8}$$

in the Z direction for each ring circuit when current I flows in the ring. The coupling factor is equal to the force induced by the actuator per unit current from Eq. (E.1). Hence, the coupling factor is expressed by

$$\alpha = B_t \cdot 2\pi r. \tag{E.9}$$

An actual coil has many turns and a number of folds. We approximately regarded the coil as a set of rings (see Fig. E.1).

Using Eq. (E.7) and Eq. (E.9), the coupling factor of the coil-magnet actuator is written as

$$\alpha = \frac{3\,\mu_0 \mathcal{M}}{2} \sum_{s=0}^{u-1} \sum_{n=0}^{w-1} \frac{(z_1 + dn)(r_1 + ds)^2}{((z_1 + dn)^2 + (r_1 + ds)^2)^{5/2}}. \tag{E.10}$$

Here, the solenoidal coil, which consists of a conductive wire with a diameter of d, is wound around a bobbin with a radius of $r_1 - d/2$. Behind the first ring, which is at a distance of $z = z_1$ from the magnet, parallel rings consisting of w turns are set with a gap of d between each ring ($z = z_1 + dn$; $n = 0, 1, 2, \cdots, w-1$). When the coil is folded into layers in the direction of increasing radius, the radius of each layer can be expressed as $r = r_1 + ds$; $s = 0, 1, 2, \cdots, u-1$ in the case of u folds. By measuring α using the relation given by Eq. (E.3), we can estimate the magnetic dipole moment, $\mathcal{M}$, using Eq. (E.10).

Bibliography

[1] A. Einstein, Ann. der Phys. **49**, 769 (1916).

[2] J.H. Taylor and J.M. Weisberg, Ap. J. **345**, 435 (1989).

[3] B.C. Barish and R. Weiss, Phys. Today **52**, No. 10, 44 (1999).

[4] B. Caron *et al.*, Class. Quantum Grav. **14**, 1461 (1997).

[5] B. Willke *et al.*, Class. Quantum Grav. **19**, 1377-1387 (2002).

[6] The Australian Consortium for Interferometric Gravitational Astronomy (http://www.gravity.uwa.edu.au/).

[7] K. Arai *et al.*, Class. Quantum Grav. **26**, 204020 (2009).

[8] M. Ando (and the TAMA Collaboration) Class. Quantum Grav. **22**, S881-9 (2005).

[9] R. Takahashi *et al.*, Class. Quantum Grav. **25**, 114036 (2008).

[10] M. Ohashi *et al.*, Class. Quantum Grav. **20**, S599 (2003).

[11] S. Miyoki *et al.*, Class. Quantum Grav. **21**, S1173 (2004).

[12] S. Miyoki *et al.*, Class. Quantum Grav. **23**, S231 (2006).

[13] M. Ohashi *et al.*, J. Phys.: Conf. Ser. **120**, 032008 (2008).

[14] K. Kuroda *et al.*, Prog. Theor. Phys. Suppl. **163**, 54 (2006).

[15] K. Numata, M. Ando, K. Yamamoto, S. Otsuka, and K. Tsubono, Phys. Rev. Lett. **91**, 260602 (2003).

[16] E.D. Black, A. Villar, and K.G. Libbrecht, Phys. Rev. Lett. **93**, 241101 (2004).

[17] H.B. Callen and T.A. Welton, Phys. Rev. **83**, 34 (1951).

[18] H.B. Callen and R.F. Greene, Phys. Rev. **86**, 702 (1952).

[19] P.R. Saulson, Phys. Rev. D **42**, 2437 (1990).

[20] G.I. González and P.R. Saulson, Phys. Lett. A **201**, 12 (1995).

[21] D.J. Dawid and S. Kawamura, Rev. Sci. Instrum. **68**, 4600 (1997).

[22] M. Kajima, N. Kusumi, S. Moriwaki, and N. Mio, Phys. Lett. A **264**, 251 (1999).

[23] A. Cavalleri *et al.*, Phys. Rev. Lett. **103**, 140601 (2009).

[24] K. Agatsuma *et al.*, Phys. Rev. Lett. **104**, 040602 (2010).

[25] G. Cagnoli *et al.*, Rev. Sci. Instrum. **69**, 2777 (1998).

[26] S. Frasca *et al.*, Phys. Lett. A **252**, 11 (1999).

[27] C.M. Mow-Lowry *et al.*, Phys. Rev. Lett. **100**, 010801 (2008).

[28] C.W. Misner, K.S. Thorne, and J.A. Wheeler, Gravitation, W.H. Freeman and Company (1970).

[29] B.F. Schutz, A First Course in General Relativity, Cambridge University Press (1985).

[30] A. Araya *et al.*, Rev. Sci. Instrum. **64**, 1337 (1993).

[31] K. Yamamoto *et al.*, J. Phys.: Conf. Ser. **32**, 418 (2006).

[32] B.J. Meers *et al.*, Phys. Rev. D **38**, 2317-2326 (1988).

[33] S Marka *et al.*, Class. Quantum Grav. **19**, 1605-1614 (2002).

[34] A. Takamori *et al.*, Class. Quantum Grav. **19**, 1615-1621 (2002).

[35] K. Agatsuma *et al.*, J. Phys.: Conf. Ser. **122**, 012013 (2008).

[36] G. Losurdo *et al.*, Rev. Sci. Ins. vol.**72**, num.9 (2001).

[37] G. Losurdo *et al.*, Class. Quantum Grav. **19**, 1631-1637 (2002).

[38] Di. Virgilio *et al.*, PRD 76, 122004 (2007).

[39] K. Yamamoto Ph D. thesis, University of Tokyo (2000).

[40] H. Nyquist, Phys. Rev. **32**, 110 (1928).

[41] A product of UNITIKA (http://www.unitika.co.jp/).

[42] T. Akutsu *et al.*, Classical Quantum Gravity **25**, 184013 (2008).

[43] T. Tomaru, T. Suzuki, T. Haruyama, T. Shintomi, N. Sato, A. Yamamoto, Y. Ikushima, T. Koyama and R. Li Class. Quantum Grav. **21**, S1005 (2004).

[44] T. Tomaru *et al.*, Cryocoolers **13**, 695 (2005).

[45] R. Li, Y. Ikushima, T. Koyama, T. Tomaru, T Suzuki, T. Haruyama, T. Shintomi and A. Yamamoto Cryocoolers **13**, 703 (2005).

[46] T. Uchiyama *et al.*, J. Phys.: Conf. Ser. **32**, 259 (2006).

[47] K. Yamamoto *et al.*, in *Proceedings of the 7th Edoardo Amaldi Conference on Gravitational Waves, Sydney, Australia, 2007*, J. Phys.: Con. Ser. **122**, 012002 (2008).

[48] K. Agatsuma *et al.*, arXiv:0911.3090 [Class. Quantum Grav. (to be published)].

[49] R.W.P. Drever *et al.*, Appl. Phys. B **31**, 97 (1983).

[50] S. Nagano *et al.*, Rev. Sci. Instrum. **74**, 4176 (2003).

[51] E. Morrison *et al.*, Applied Optics, **33**, Issue 22, pp.5037-5040 (1994).

[52] E. Morrison *et al.*, Applied Optics, **33**, Issue 22, pp.5041-5049 (1994).

[53] H. Hirakawa *et al.*, Physics Letters **63A**, 199 (1977).

[54] A. Vinante *et al.*, Phys. Rev. Lett. **101**, 033601 (2008).

[55] K. Numata, A. Kemery, and J. Camp, Phys. Rev. Lett. **93**, 250602 (2004).

[56] Details are in *Gravitational Wave Detection*, edited by K. Tsubono, M.-K. Fujimoto, and K. Kuroda (University Academy Press, Tokyo, 1997).

[57] A product of DAIKIN (http://www.daikin.co.jp/index.html).

[58] A product of JECC TORISHA Co., Ltd (http://www.jecctorisha.com/index.html).

[59] Gerhard Heinzel, *TAMA coil driver modification*, TAMA Project, (2000).

[60] K. Yamamoto *et al.*, Phys. Rev. D **74**, 022002 (2006).

[61] M. Hewitson *et al.*, Class. Quantum Grav. **24**, 6379-6391 (2007).

[62] K. Yamamoto, M. Ando, K. Kawabe, K. Tsubono, Phys. Lett. A **305**, 18-25 (2002).

Acknowledgements

This work was supported in part by Global COE Program "the Physical Sciences Frontier", MEXT, Japan and in part by a JSPS Grant-in-Aid for Scientific Research (No. 18204021).

I am grateful to everyone who gave me helpful advices. The main theme of this thesis originated from the noise hunting of CLIO by Professor Kawamura. He proposed the replacement of the coil holder because he suspected that the eddy currents in the conductive coil holder degraded the Q-factor of the pendulum. This noise hunting was performed in only two days, and I admire his insight. My supervisor Prof. Ohashi led me to the study of CLIO. I am greatly thankful for his sharp and kindhearted advices. I am much obliged to Dr. Uchiyama, Dr. Miyoki, and Dr. Miyakawa for their support of the experiments in CLIO. I cannot thank Dr. K. Yamamoto enough. He advised me many times on theoretical discussions, the manuscripts of published papers, and this thesis. I would also like to thank Dr. H. Yamamoto for some helpful comments on this manuscript and on helping in the reply to the referees of the submitted paper. I would like to thank Dr. Shiomi for some comments she made on this manuscript. I would like to appreciate K. Ishidoshiro, K. Takahashi, N. Ohmae and every my friend for many discussions. I am most grateful to my family for everything.